ENHANCING THE VOLUMETRIC EFFECT OF POINT-FOCUSING CONCENTRATING SOLAR RECEIVERS VIA PARTIALLY REFLECTIVE SURFACES

A Thesis

by

FATHYA YOUSIF MOHAMED SALIH

Submitted to the Graduate and Professional School of
Texas A&M University
in partial fulfillment of the requirements for the degree of

MASTER OF SCIENCE IN CHEMICAL ENGINEERING

Chair of Committee,	Konstantinos Kakosimos
Committee Members,	Ahmed Abdala
	Arun Srinivasa
Head of Department,	Patrick Linke

December 2021

Major Subject: Chemical Engineering

Abstract

One of the remaining challenges of point focusing concentrating solar power systems is the realization of a true volumetric receiver, one whose entire volume is utilized for the absorption of irradiance. Current state-of-the-art receivers (e.g., HiTRec-II and SolAir-200) have not demonstrated the volumetric effect, because of low radiation penetration within the absorber. Earlier works have noted that radiation penetration can be improved by increasing porosity (void fraction), but at the cost of reducing the convective heat transfer area. More recent works have succeeded at improving radiation penetration in volumetric absorbers by axially grading the porosity of the structure, but those designs are complex and share the issue of manufacturability. Nevertheless, the improvements are notable and justify the pursuit of true volumetric receivers. This work discusses the conceptual design and numerical evaluation of a true volumetric receiver achieved by applying different reflectivity distributions to the irradiated surfaces to improve radiation penetration.

The square honeycomb receiver structure was reduced to a single channel to allow for detailed modelling of radiative phenomena. Monte Carlo ray tracing was used to model external irradiance and the conventional direct integration approach was used to model mutual irradiance. This radiative model was coupled with a 3-dimensional heat transfer model and a laminar flow model for a complete description of the problem. Furthermore, the relationship between the axial reflectivity distribution and relevant design parameters like porosity and residence time are explored via parametric sweeps, with solar-to-thermal efficiency exit gas temperature and the volumetric effect ratio as the monitored responses. This work was completed using COMSOL Multiphysics®.

The base case parametric study showed that the optimal parameters for a Silicon Carbide uniform reflectivity receiver are those of the HiTRec-II. Both varied reflectivity receiver cases considered exhibited an improvement in performance parameters for the same average emissivity of the base case. The best performance was achieved by a wall-varied reflectivity receiver, where every two walls were assigned a certain emissivity based on the amount of radiation they intersect. This receiver design is expected to achieve an increase of 5.2%, 6.1% and 8.2% in the exit gas temperature, thermal efficiency and volumetric effect, respectively, compared to the HiTRec-II.

Contributors & Funding Sources

Contributers

This work was done under the supervision of a thesis committee consisting of Dr. Konstantinos Kakosimos and Dr. Ahmed Abdala from the Department of Chemical Engineering at Texas A&M University at Qatar and from Dr. Arun Srinivasa from the Department of Mechanical Engineering at Texas A&M University, College Station.

All other work conducted for the thesis was completed by the student independently.

Funding Sources

Graduate study was supported by a fellowship from Texas A&M University at Qatar. This work was also made possible in part by a NPRP award [NPRP12S-0301-190191] from Qatar National Research Fund (QNRF).

Abbreviations & Nomenclature

Mathematical & Greek Symbols:	*Subscripts:*
T ≡ absolute temperature [K]	g ≡ gas domain (bulk)
ρ ≡ density [kg/m^3]	s ≡ solid domain
C_p ≡ heat capacity at constant pressure [J/kg]	avg ≡ average property
k ≡ thermal conductivity [W/(m·K)]	in ≡ property at the inlet
$\mathbf{u}$ ≡ velocity vector [m/s]	out ≡ property at the inlet
p ≡ pressure [atm]	*Abbreviations:*
μ ≡ dynamic viscosity [Pa.s]	CSP ≡ Concentrating solar power
$\boldsymbol{F}$ ≡ bulk forces acting on a unit fluid volume [N/m^3]	DNI ≡ Direct normal irradiance
$\boldsymbol{K}$ ≡ viscous stress tensor [Pa]	FDM ≡ Finite difference method
σ ≡ Stefan-Boltzmann constant [5.67×10^{-8} W/(m^2.K^4)]	FEM ≡ Finite element method
n ≡ refractive index [-]	
ε ≡ surface emissivity [-]	
α ≡ surface absorbtivity [-]	

Table of Contents

List of Tables

List of Figures

1. Introduction

1.1 Background & Motivation

To face the persistent challenges of global warming and increasing global energy demands, research efforts in the past few decades have focused on routes to utilizing different sources of renewable energy. One route that proved to be promising in large-scale tests is Concentrated Solar Power (CSP). A CSP plant consists of a system of reflectors that focus radiation onto a solid receiver, where radiative energy is absorbed by the solid and transferred by convection to a working fluid for either thermal storage or conversion into electricity. CSP's compatibility with cheap thermal storage and well-developed thermal-to-electrical thermodynamic cycles highlight the technology's significance and potential (Köberle, Gernaat and van Vuuren, 2015).

Based on the concentrator configuration, CSP systems can be broadly categorized into line-focusing (or tube-receiver) systems and point-focusing (or central receiver) systems. Point-focusing CSP systems are of more interest, because their higher concentration ratios can achieve higher HTF temperatures and in turn greater solar-to-electric efficiencies (Ávila-Marín, 2011). Subsequently, the design and optimization of the receiver system – where the solar-to-thermal energy conversion occurs – is a key area of research in central CSP.

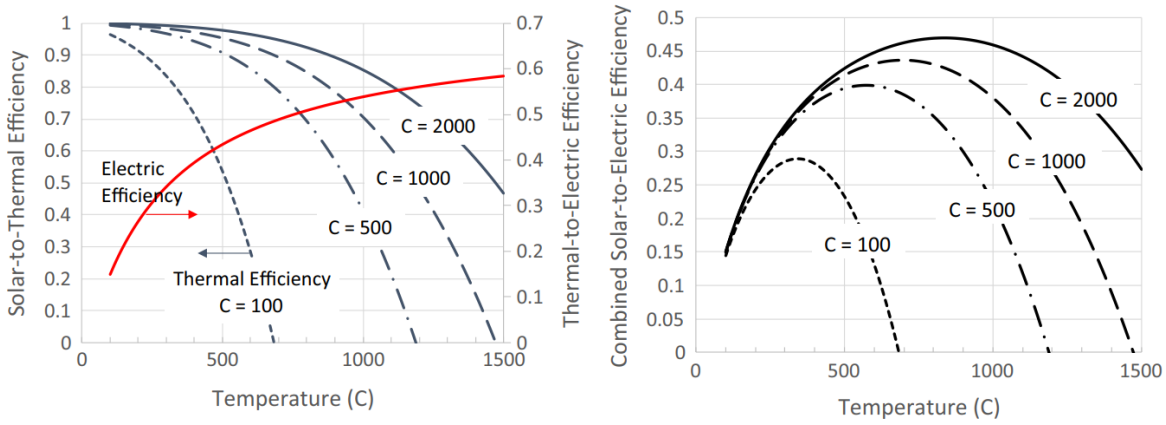

Figure 1.1: Temperature-dependence of solar-to-thermal and thermal-to-electric efficiency (left), and effect of concentration ratio on overall efficiency (right). Recreated from Ho (2017)

Volumetric receivers, commonly used in central CSP systems, are porous structures that receive concentrated radiation and the HTF through the same inlet port and utilize the entire receiver's volume to absorb radiation. However, state of the art of volumetric receivers like HiTRec-II and SolAir-200 did not fully utilize the receiver volume. 90% of the radiation was absorbed in the front 20% of the receiver for an absorber modelled by (Alberti *et al.*, 2016) based on the dimensions of the SolAir-200. Full utilization of receiver volume is characterized by the volumetric effect, where it is expected that the temperature of the receiver at the inlet would be lower because of convective cooling, minimizing re-radiation losses and improving thermal efficiency (Kribus *et al.*, 2014).

In an effort to realize the volumetric effect, studies have looked into the influence of bulk or effective properties on the temperature profiles and efficiency of volumetric absorbers. (Kribus et al., 2014) noted that increasing porosity and pore size improved radiative penetration and, hence, thermal efficiency, but not to a significant extent. A greater volumetric effect was achieved by increasing the volumetric HTC. However, volumetric surface area and porosity have an inverse relationship, and optimal performance in a uniform-property volumetric receiver is typically a tradeoff between improving radiative penetration and increasing specific surface area.

To overcome this tradeoff, some works have attempted axially varying the porosity of volumetric receivers to create a front region that improves radiative penetration and a back region that enhances convective transport. (Avila-Marin, Alvarez de Lara and Fernandez-Reche, 2018) attempted a discretely varied design by axially stacking metallic meshes of different porosities. (Du, Ren and He, 2017) modelled and optimized a foam receiver with gradually varying porosity (from 0.95 to 0.65, inlet to outlet). Both studies reached a similar conclusion, the greatest increase in thermal efficiency is obtained when a high, almost constant, porosity in the front 70% of the receiver is followed by a sudden drop in the back end. However, these implementations of the concept did not achieve the volumetric effect.

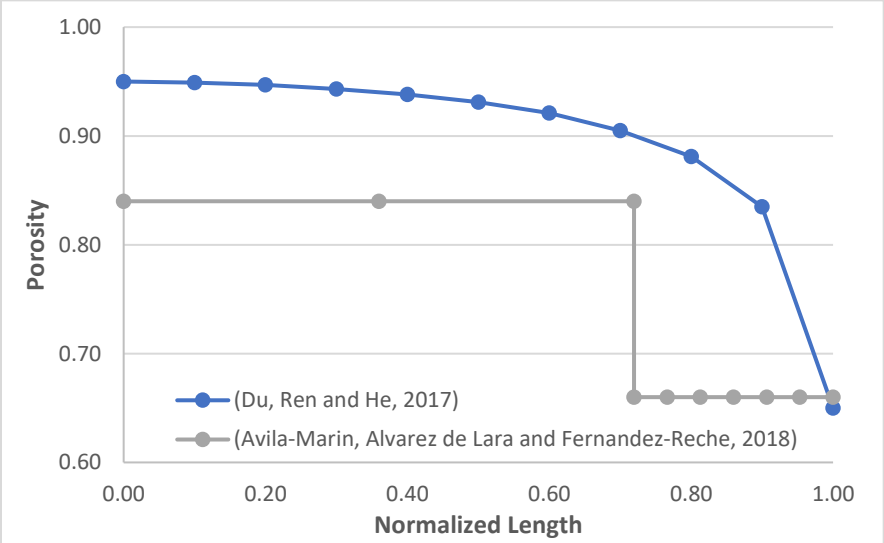

Figure 1.2: Optimized graded porosity distributions in literature ((Avila-Marin, Alvarez de Lara and Fernandez-Reche, 2018) and (Du, Ren and He, 2017))

Additionally, radially varied porosity (higher at the center) in foam receivers can improve radiative penetration when a gaussian incident flux distribution is considered (Du *et al.*, 2020). This does not attain the volumetric effect, either.

A group of axially varied porosity receivers that deserves distinction is fractal-like structures, which are inspired by the porcupine and other modified tube receivers that add fin-like structures

to the irradiated surface to increase light-trapping (tube receiver examples include (Lubkoll, Von Backström and Harms, 2016) (Wang *et al.*, 2016) and (Ortega *et al.*, 2016)). (Luque *et al.*, 2018) tested a fractal-like volumetric receiver made from layers of repeated 2D elements arranged on different 3D planes with layer-porosity ranging from 0.87 in the front to <0.50 in the back. And (Capuano *et al.*, 2017) demonstrated a honeycomb-like structure that gradually phases the porosity from 0.97 in a front pin-shaped section to 0.71 in a backing honeycomb section. Both the designs mentioned successfully achieved the volumetric effect, but the developed complex designs prohibit using the high-performance ceramics desired in volumetric receivers with currently available layered manufacturing techniques.

Furthermore, one approach that has only been considered once in literature is axially varied reflectivity. (Ali *et al.*, 2020) modeled a high reflectivity honeycomb receiver and applied a high absorbance coating (Pyromak 2500) to the back half of each channel. Though improved volumetric behavior is reported, the solid temperature exceeded the gas exit temperature only 20% into the receiver. This shows the approach has some potential to achieve the volumetric effect with the appropriate optimized design.

Taking clues from the literature, this work focuses on modeling and optimizing a honeycomb volumetric receiver with an imposed reflectivity distribution on the irradiated surfaces to realize the volumetric effect. A 3D CFD model with surface-to-surface radiation is developed for a hexagonal-channel honeycomb receiver. The receiver is reduced to a single channel to minimize computational effort and allow for detailed radiation modeling, a common approach for modeling structured receivers (Sedighi *et al.*, 2020). The design proposed is expected to attain the volumetric effect and exceed the efficiencies of current state of the art receivers, while remaining simple, robust and manufacturable.

Table 1.1: Summary of literature survey – attempts at achieving the volumetric effect

Receiver Material	Geometry	Specific Surface Area (m^2/m^3)	Porosity	Extinction Coefficient (m^{-1})	Performance	Reference
-	Multi-layer staggered square grid absorber	-	-	-	Reflective losses increased by 3% η_{th} no reported	(Gomez-Garcia *et al.*, 2015)
-	honeycomb with cutback features in the front face	-	-	-	-	(Nakakura *et al.*, 2018)
Metallic (iron-based alloy 1.4767)	Exhaust engine reactor with cut wings and perforations in each channel	-	> 0.90	-	Gas temp. of 800°C at solid temp. of 950°C	(Pabst *et al.*, 2017)
Ceramic (SiC)	Foam – axially graded porosity distribution	-	0.95 – 0.65	802.2	Improved radiative penetration	(Du, Ren and He, 2017)
Metallic (SS 601)	Meshes of different sizes stacked on each other	-	-	-	η_{th}^{max} = 87% (D)	(Avila-Marin, Alvarez de Lara and Fernandez-Reche, 2018)
Metallic (Inconel 718)	Foam – radially graded porosity distribution	510	0.80 (avg)	502.2	η_{th}^{max} = 87% (D)	(Du *et al.*, 2020)
Metallic (Ti_6Al_4V)	Fractal-like – graded porosity with pin-shaped front and a honeycomb back	318 – 870 (D) 990 – 2860 (S)	0.97 – 0.71	-	η_{th}^{max} = 84% (D – at $^{P}/_{\dot{m}}$ 700) η_{th}^{max} = 80% (D - Projected)	(Capuano *et al.*, 2017)
Metallic (AISI 316L SS)	Fractal-like – repeating 2D elements on 3D planes	420 – 950	0.97 – 0.48	-	η_{th}^{max} = 83% (D)	(Luque *et al.*, 2018)
Ceramic (partially coated alumina)	Honeycomb – square channel partially coated w/ Pyromak 2500	-	-	-	79% (S – at unknown conditions)	(Ali *et al.*, 2020)

1.2 Objectives

1. To model a base case honeycomb volumetric receiver and verify the model using literature data for the current state-of-the-art in volumetric receivers, the HiTRec-II.
2. To evaluate the performance of graded-reflectivity honeycomb receivers of square and hexagonal channel geometries.
3. To find an optimal performance varied-reflectivity receiver and compare its performance to that of the HiTRec-II.

2. Methodology

The following section describes the tools and methods used to perform this work. It starts with a brief description of the phenomena involved in the system at hand and highlights the key assumptions used to reduce/simplify the problem. The energy and momentum transport equations are described along with their respective boundary and initial conditions. Then, two implementation approaches attempted in this work – the conduction equation solved using finite differences and the momentum and energy equations solved using the finite element method –are described. Furthermore, the system description and reference cases used to verify each implementation attempt are detailed. Finally, the parameters, responses, and methods used to conduct the sensitivity analysis and optimization are discussed.

2.1 System Reduction & Geometry

Central CSP receivers, especially open air SPT receivers like the HiTRec-II and SolAir-200, are generally assembled in a modular fashion like in Figure 2.1 below. In operation, each module is assumed to have a discrete value for the power on aperture (P), according to a discretized distribution of the flux incident from the concentrator field (Hoffschmidt *et al.*, 2003). The mass flux through the module ($\dot{m}$) is, then, determined from the desired power on aperture to mass flux ratio ($P/\dot{m}$) for that module to maintain a similar exit gas temperature from all modules. Meaning, a central CSP receiver can be reduced to a single module operating under a given power on aperture to mass flux ratio.

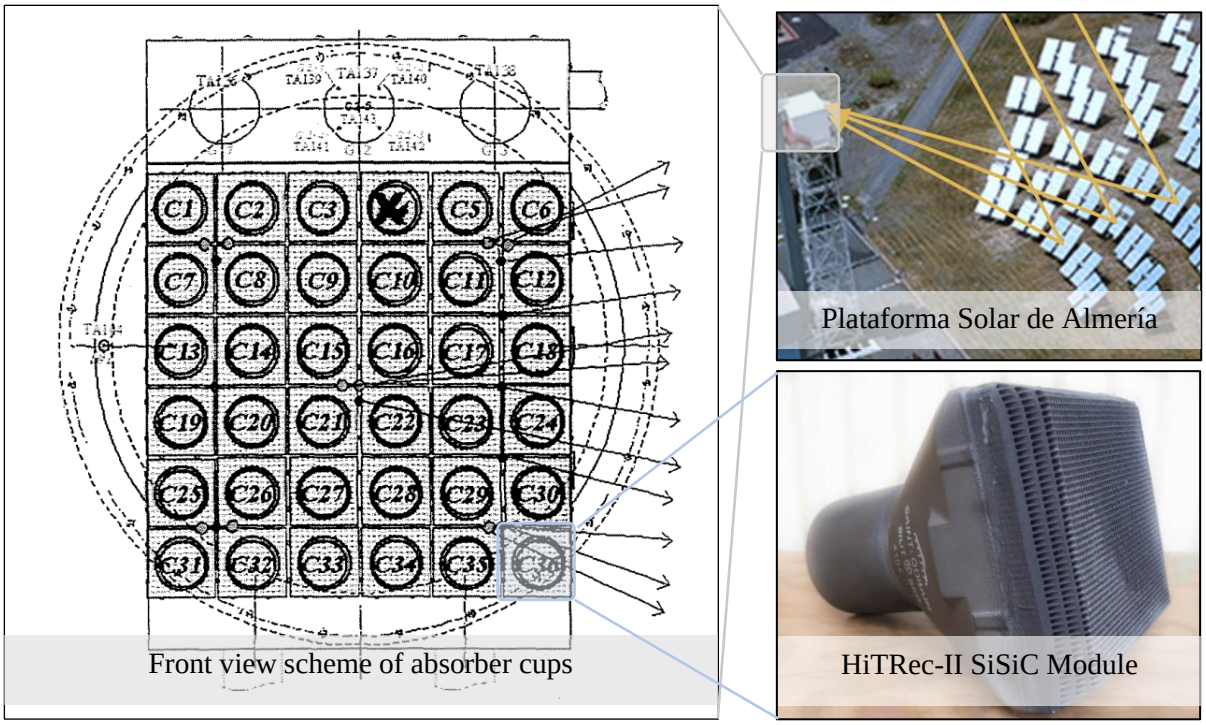

Figure 2.1: SolAir-200 kWth absorber configuration

Furthermore, a single receiver module can be further reduced to a single channel with adiabatic external walls, assuming the radiative flux on the module aperture is uniformly distributed. This allows a discrete treatment of radiative transfer, which has been proven to have a greater impact on model accuracy than different momentum transport modeling approaches (Capuano *et al.*, 2016). The figure below shows the geometry of the receiver/s considered with the HiTRec-II as an example. The actual shape of the channel is allowed to vary in different studies, but the definitions of the dimensions do not change.

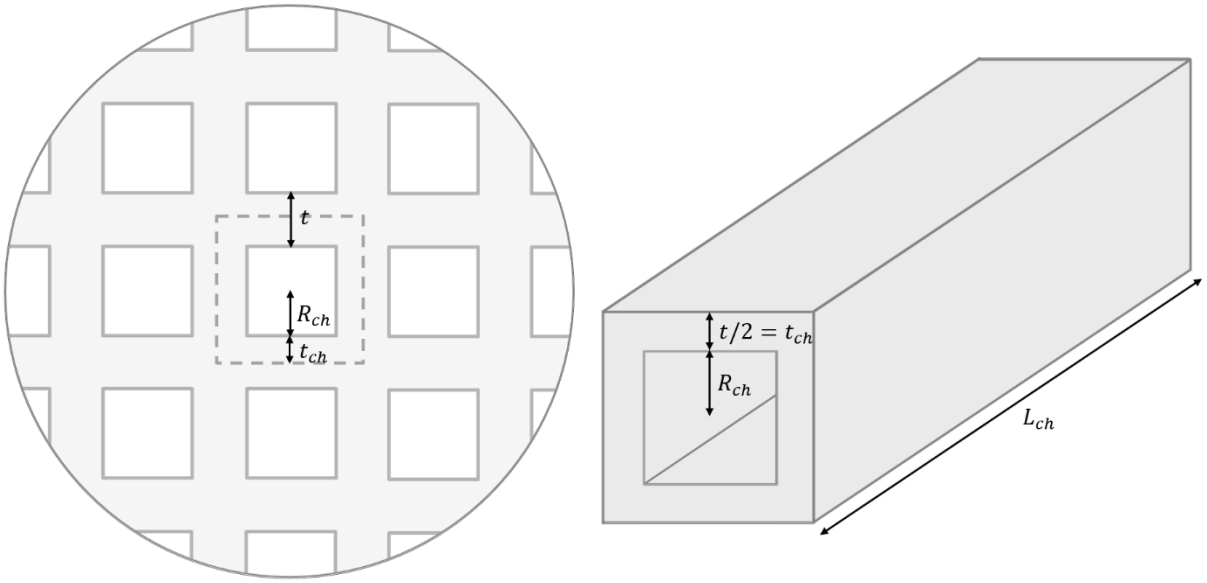

Figure 2.2: Geometry, system reduction and system dimensions

Where R_{ch} ≡ radius of a cylinder inscribed in the channel [mm]

L_{ch} ≡ length of channel [mm]

t ≡ wall thickness (for the whole receiver) [mm]

t_{ch} ≡ channel thickness (after geometry reduction) [mm]

2.2 Domain Transport Equations

2.2.1 Energy Transport Equations

The most useful form of the energy equation is written in terms of temperature as an equation of change for the total energy. It is derived as the sum of the conservation equations for internal energy 'e' and kinetic or mechanical energy 'K' yielding eqn. **Error! Reference source not found.** below (Bird, Stewart and Lightfoot, 2002).

$$\frac{\partial(\rho E)}{\partial t} = -\nabla \cdot (\rho \mathbf{u} E) - \nabla \cdot \mathbf{q} + Q + \nabla \cdot (\sigma \cdot \mathbf{u}) + \rho \mathbf{g} \cdot \mathbf{u} \qquad 1$$

Where $E = e + K = C_p T + {}^1/_2\,(\mathbf{u}\cdot\mathbf{u})$

$\mathbf{u} \equiv$ velocity vector of translational motion [m/s]

$\mathbf{q} \equiv$ diffusive heat flux (i.e. conductive flux) [W/m^2]

$\sigma \equiv$ work done per unit volume (i.e. molecular stress) [J/m^3]

$Q \equiv$ additional volumetric energy sources [W/m^3]

Applying this equation to the solid domain, all terms containing translational motion are cancelled, since the solid is stationary relative to the system coordinates ($\mathbf{u} = 0$). Also, no additional heat sources are present and the conductive flux ($\mathbf{q}$) can be substituted using Fourier's law, leaving:

$$\rho_s\, C_{p,s} \frac{\partial T_s}{\partial t} = \nabla\cdot(k_s\cdot\nabla T_s) + Q \qquad 2$$

Here, the source term 'Q' is net radiative flux and is applied only at the irradiated boundaries and its calculation is covered in section 0.

Furthermore, eqn. **Error! Reference source not found.** for the fluid will include the fluid flow field '$\mathbf{u}$' and the total molecular stress 'σ', which would be decomposed to a normal stress and a shear stress component ($\sigma = \boldsymbol{\tau} - p\mathbf{I}$). Also, there are no volumetric source terms acting in the fluid phase since the gas is assumed to be a non-participating medium. Thus, the energy equation for the fluid is written as in equation 3 below (Bird, Stewart and Lightfoot, 2002).

$$\rho_g \frac{\partial}{\partial t}\left(C_{p,g}T_g + \frac{1}{2}\,(\mathbf{u}\cdot\mathbf{u})\right) = -\rho_g\nabla\cdot\left(\mathbf{u}\left(C_{p,g}T_g + \frac{1}{2}\,(\mathbf{u}\cdot\mathbf{u})\right)\right) + \nabla\cdot\left(k_g\cdot\nabla T_g\right) - \nabla\cdot p\mathbf{u} - \nabla\cdot(\boldsymbol{\tau}\cdot\mathbf{u}) + \rho_g\,\mathbf{g}\cdot\mathbf{u} \qquad 3$$

However, in this problem it is assumed that viscous dissipation is minimal due to the low dynamic viscosity of air. And the effects of gravity on the total mechanical energy can be neglected, yielding equation 4 below.

$$\rho_g \frac{\partial}{\partial t}\left(C_{p,g}T_g + \frac{1}{2}(\mathbf{u}\cdot\mathbf{u})\right) = -\rho_g \nabla\cdot\left(\mathbf{u}\left(C_{p,g}T_g + \frac{1}{2}(\mathbf{u}\cdot\mathbf{u})\right)\right) + \nabla\cdot\left(k_g\cdot\nabla T_g\right) - \nabla\cdot p\mathbf{u} \qquad 4$$

2.2.2 Radiative Transport Equations

1. Direct-Integration Approach

Since the medium is assumed to be non-participating and each irradiated surface element is opaque, diffuse and of uniform temperature, surface-to-surface radiation (S2SR) model can be used. In it, the net radiative flux leaving a surface element 'i' can be obtained by applying an energy balance at the surface, as in Figure 2.3. For a diffuse surface, this simplifies to the difference between the surface radiosity (J_i) and the irradiance on the surface (I_i), as in equation 5 below (Incropera *et al.*, 2007).

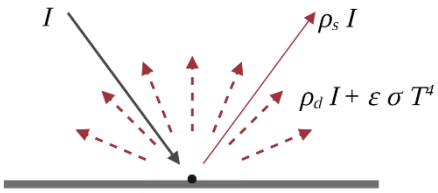

Figure 2.3: Radiative energy balance on a partially specular and partially diffuse surface

$$q_i = J_i - I_i \qquad 5$$

Here, radiosity is the sum of all diffuse radiation leaving a surface element and can be described by eqn. 6 below.

$$J = \rho_d I + \varepsilon n^2 \sigma T_s^4 \qquad 6$$

Where 'ρ_d' is the diffuse reflectivity and 'I' is the sum of all radiation incident on the surface element 'i' including mutual irradiance emitted by other surface elements in the enclosure (I_m), ambient irradiance (I_{amb}) and that coming from external radiation sources (I_{ext}) (COMSOL Multiphysics®, 2020b).

$$I = I_m(F_m, J) + I_{ext}(F_{ext}, P_s) + I_{amb}(F_{amb}, \varepsilon_{amb}, T_{amb}) \qquad 7$$

View factors for radiosity calculation (F_m, F_{amb}) are evaluated using the Hemicube method. A direct integration method that is based on the principle that all projections of a viewed surface element have the same form factor. This is illustrated in

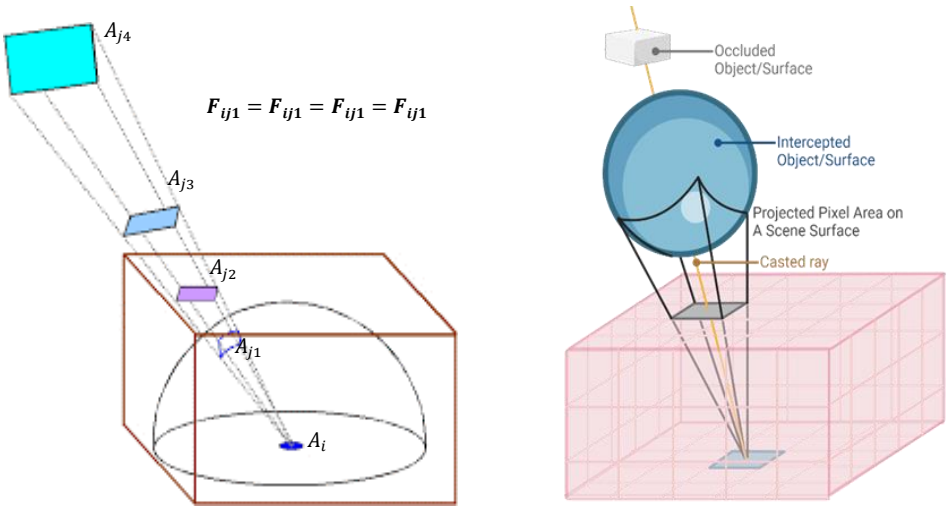

Figure 2.4 where a viewed hemisphere element has the same view factor as its projection onto an enclosing hemicube (Gillies, 2018).

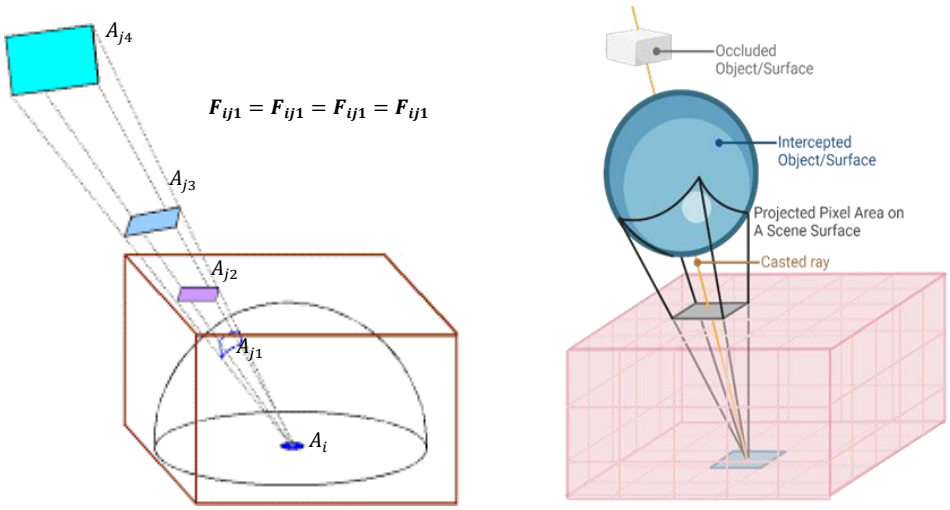

Figure 2.4: Hemicube method description. Left: Hemicube method principle recreated from (Gillies, 2018), Right: Occlusion of surface elements in hemicube method

A unit hemicube (half of a cube) is generated around a specific surface element 'i' to represent its view field. And the image seen by element 'i' is the projection of the scene on the pixels of the hemicube surface. One ray emitted from the center of element 'i' is generated to pass through the center of each pixel in the hemicube. The first time one of those casted rays is intersected by another surface element in the geometry 'j', it is assumed that all elements of the geometry in the direction of that ray are occluded by the intersected element 'j' (i.e. the view factor between 'i' and all other elements other than 'j' is zero). This assumption becomes more accurate as the resolution or number of the hemicube pixels is increased. The overall form factor can be calculated as the sum of the delta form factors (ΔF_{ij} – form factor per pixel) shown in eqn. 8 below. This simplifies similar methods like the hemisphere method because the pixel area for all elements is equal and view angles ϕ_i and ϕ_j are easy to correlate and calculate (Gillies, 2018).

$$F_{ij} = \sum_j \Delta F_{ij} = \frac{\cos\phi_i \cos\phi_j \ \Delta A}{\pi r^2} \qquad 8$$

2. Statistical Approach (Monte Carlo Ray Tracing)

Evaluating the irradiance of an external radiation source, whether it be a heliostat field or a high flux solar simulator, would require a high computational cost using direct integration methods. For systems of this level of complexity, it is preferred to use statistical techniques like Monte Carlo Ray Tracing (MCRT) to evaluate view factors or directly measure I_{ext} on an element.

Monte Carlo simulations are a large class of probabilistic methods used to solve deterministic problems where the direct solution of moderately complex problems requires a prohibitive amount of computational time (see Figure 2.5 below for reference) (Modest, 2013).

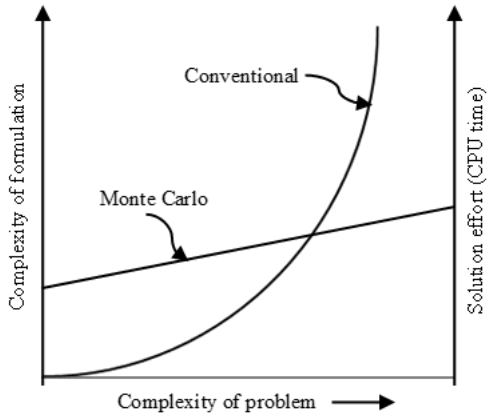

Figure 2.5: CPU time for Monte Carlo and direct integration methods – recreated from (Modest, 2013)

The loop for tracing one ray using MCRT is as shown in Figure 2.6 below. In it, a ray is defined by an origin point 'r_0' and a direction unit vector '$\hat{u}$'. All ray-boundary intersections are calculated by equating the ray equation (eqn. 9 below) to the surface equation for each boundary (eqn. 10 below) and solving for the ray length parameter 't'. The nearest ray-boundary intersection is the one used to calculate the new ray direction based on the boundary's optical properties. Depending on the medium properties, the ray power and/or intensity can dissipate as it travels through the medium, but its direction (or equation) will not change till it intersects a boundary. A boundary is any opaque or semi-transparent surface that can change the ray's direction (e.g. a metal surface or

a fluid-fluid interface). The tracing loop for a single ray is terminated when it is absorbed by another surface element or exits the geometry (Sarwar *et al.*, 2015).

$$P = r_0 + t\ \hat{u} \tag{9}$$

$$(P - p_0) \cdot \hat{n} = 0 \tag{10}$$

$$t = -\frac{(r_0 - p_0) \cdot \hat{n}}{\hat{u} \cdot \hat{n}} \tag{11}$$

Where $p_0 \equiv$ plane center (or any point on the plane) for traced surface

$\hat{n} \equiv$ plane normal for the traced surface

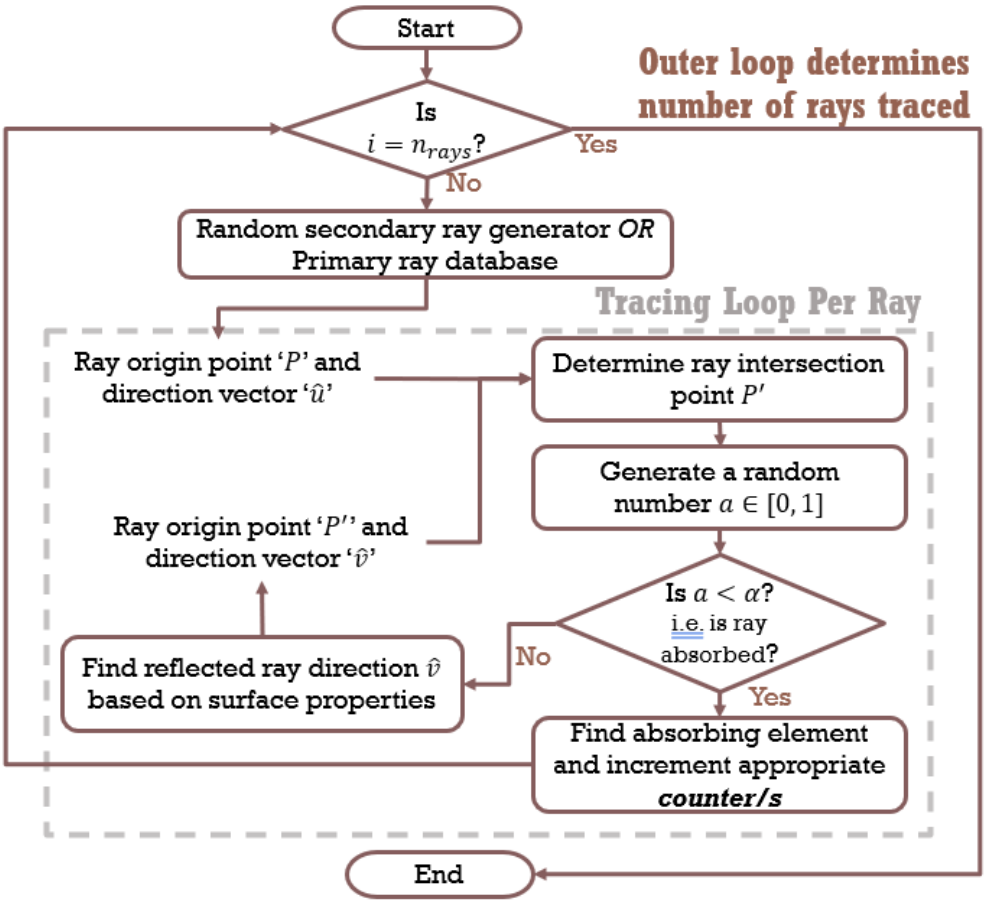

Figure 2.6: Algorithm for Monte Carlo ray tracing (MCRT)

When a surface element 'i' absorbs a ray, the external irradiance (I_{ext}) on that element is incremented by the power of the absorbed ray. However, since the medium in this problem is considered non-participating, the power of a ray is not expected to change significantly from emission to absorption and only the number of primary rays (emitted by external sources) needs to be accumulated for each surface element.

$$I_{ext}|_i = n_{ab,i} * P_{p,ray} \qquad 12$$

Where $n_{ab,i} \equiv$ no. of absorbed primary rays by element 'i'

$P_{p,ray} \equiv$ power per primary ray [W]

2.2.3 Momentum Transport Equations

The Navier-Stokes equation is a form of the equation of motion derived from molecular arguments by Navier and from continuum arguments by Stokes. For a Newtonian fluid, where the viscous stress tensor is ($\boldsymbol{K} = \mu(\nabla\mathbf{u} + (\nabla\mathbf{u})^T) = \mu\nabla\mathbf{u}$), the NVE take the following form:

$$\rho_g \frac{\partial \mathbf{u}}{\partial t} + \rho_g(\mathbf{u}\cdot\nabla)\mathbf{u} = -\nabla\cdot p\boldsymbol{I} + \nabla\cdot[\mu\nabla\mathbf{u}] + \boldsymbol{F} \qquad 13$$

Where $\mu \equiv$ dynamic viscosity [Pa.s]

$\boldsymbol{F} \equiv$ the volume or bulk force vector [N/m^3]

Because of the low density of the fluid, gravity effects are excluded. Buoyant forces can be added as a momentum source term using the Boussinesq approximation. It assumes that the temperature dependence of density only affects the gravity or bulk force term yielding equation 15, known as the Boussinesq equation of motion. However, in cases where the acceleration term. '$(\partial\mathbf{u}/\partial t + (\mathbf{u}\cdot\nabla)\mathbf{u})$' is comparable to gravitational acceleration '$\mathbf{g}$' (i.e. cases where natural and

forced convection effects are both significant). The temperature dependence of density is included in both acceleration terms, yielding equation 16 below (Bird, Stewart and Lightfoot, 2002).

$$\rho_g(T) = \bar{\rho}_g - \bar{\rho}_g\,\bar{\beta}\,(T - \bar{T}) \tag{14}$$

$$\rho_g \frac{\partial \mathbf{u}}{\partial t} + \rho_g(\mathbf{u}\cdot\nabla)\mathbf{u} = -\nabla\cdot p\boldsymbol{I} + \nabla\cdot[\mu\nabla\mathbf{u}] + \left(\bar{\rho}_g - \bar{\rho}_g\,\bar{\beta}\,(T - \bar{T})\right)\mathbf{g} \tag{15}$$

$$\left(\rho_g - \bar{\rho}_g\right)\left(\frac{\partial \mathbf{u}}{\partial t} + (\mathbf{u}\cdot\nabla)\mathbf{u}\right) = -\nabla\cdot p\boldsymbol{I} + \nabla\cdot[\mu\nabla\mathbf{u}] + \left(\bar{\rho}_g - \bar{\rho}_g\,\bar{\beta}\,(T - \bar{T})\right)\mathbf{g} \tag{16}$$

Where $\bar{\rho}_g \equiv$ fluid density at the average wall temperature $\bar{T}$ [kg/m^3]

$\bar{T} \equiv$ average temperature of walls considered in the direction of buoyant force [K]

$\bar{\beta} = -1/\rho\,(\partial\rho/\partial T)_p \equiv$ thermal expansion coefficient evaluated at $\bar{T}$ [1/K]

These equations (components of eqn. 16) need to be solved under the restriction of the continuity equation (or the overall mass balance) below.

$$\frac{\partial \rho_g}{\partial t} + \nabla\cdot\left(\rho_g\mathbf{u}\right) = 0 \tag{17}$$

For an incompressible flow like the one assumed here, the time derivative of density disappears and the continuity equation becomes:

$$\nabla\cdot\mathbf{u} = 0 \tag{18}$$

2.3 Initial and Boundary Conditions

2.3.1 Initial Conditions

All temperature nodes are assumed to start at the ambient temperature. The initial conditions for the momentum equations are that the fluid is stationary, and the pressure is equal to the ambient pressure.

2.3.2 Boundary Conditions

2.3.2.1 Exterior Channel Walls

All exterior channel walls parallel to the direction of flow are under an adiabatic boundary condition because of thermal symmetry according to the following expressions:

$$\mathbf{q}_{\mathbf{cond}} = 0 \qquad 19$$

$$\nabla T_s = 0 \qquad 20$$

These walls, also, are not physically exposed to the system's surroundings and do not participate in radiative transfer (i.e. they do not emit, absorb or reflect radiation). Any rays intersecting these walls are terminated and treated as though they had exited the geometry without interaction.

2.3.2.2 Interior Channel Walls

The interior channel walls in the solid domain are exposed to conduction, forced convection, deposited radiative power, and reradiated energy flux for the energy equation. This can be considered a system boundary for the energy equation when the energy equations for the solid and fluid domains (equations 2 and 4, respectively) are solved separately. In that case, the boundary

condition at the interface for those equations would be described according to equations 21 & 22 below, which results from the energy balance at the surface as shown in Figure 2.7 below.

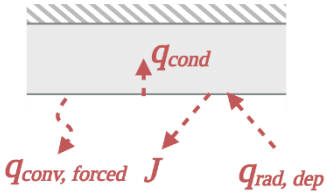

Figure 2.7: Energy balance at the gas-solid interface

$$\mathbf{q_{cond}} + \mathbf{q_{rad,dep}} - \frac{J}{A} - \mathbf{q_{conv,f}} = 0 \qquad 21$$

$$-k_s \nabla T_s + \mathbf{q_{rad,dep}} - \frac{J}{A} - h_f\left(T_s - T_{g,b}\right) = 0 \qquad 22$$

Alternatively, the general form of the energy equation (eqn. 1) can be applied for both domains, leaving the gas-solid interface as an interior part of the system that is, trivially, defined by continuity according to equation 23 below.

$$T_s = T_g \qquad 23$$

Additionally, the boundary condition for the momentum equation at this interface is the no-slip condition defined by equation 24. And, finally, the boundary condition for MCRT at this wall is diffuse scattering. Wherein, equations 25 and 26 show how the ray counters are updated depending on whether the ray being traced is absorbed or reflected. Equation 27 determines the angle of reflection for the ray, where the condition ($\hat{u}_{refl} \cdot \hat{n} \geq 0$) requires that the ray is reflected into the positive normal direction of the intersected plane. If the reflected ray direction does not satisfy this condition, the randomly generated ray direction is simply mirrored.

$$\mathbf{u} = 0 \tag{24}$$

$$n_{rays,abs} = \begin{cases} n_{rays,abs} + 1 & if\ a_1 < \alpha \\ n_{rays,abs} & if\ a_1 \geq \alpha \end{cases} \tag{25}$$

$$n_{rays,refl} = \begin{cases} n_{rays,refl} & if\ a_1 < \alpha \\ n_{rays,refl} + 1 & if\ a_1 \geq \alpha \end{cases} \tag{26}$$

$$\theta_{refl} = a_2 * 2\pi \ \leftrightarrow \ \hat{u}_{refl} \cdot \hat{n} \geq 0 \tag{27}$$

Where $n_{rays,abs}$ ≡ the number of rays absorbed by the intersected surface element

$n_{rays,refl}$ ≡ the number of rays reflected by the intersected surface element

$a_1, a_2, etc.$ ≡ random numbers in the period [0,1]

$\hat{u}_{refl}$ ≡ reflected ray direction vector (normalized)

2.3.2.3 Front Face of Channel Receiver

The front face of the receiver is exposed to ambient air and concentrated radiation. Contact with ambient air causes heat loss by natural convection and radiation at that surface. Because the contribution of natural convection to heat loss at the front face is less significant than radiative losses, natural convection is only modeled by a constant heat transfer coefficient (h_{nat}) in the range 0 to 10 W/m^2·K. A practice followed by many previous works ((Ho, 2017), (Ali *et al.*, 2020), (Usman and Ozalp, 2012)). Radiation losses are modeled using the Stefan-Boltzmann law for exchange between diffuse gray surfaces, and the deposited ray power is calculated as in equation 12. Hence, the final energy balance at the boundary becomes:

$$\mathbf{q_{cond}} + \mathbf{q_{rad,dep}} - \mathbf{q_{conv,nat}} - \mathbf{q_{rad,amb}} = 0 \quad (28)$$

$$-k_s \nabla T_s + \mathbf{q_{rad,dep}} - h_{nat}(T_s - T_{amb}) - \varepsilon\sigma\left(T_s^4 - T_{amb}^4\right) = 0 \quad (29)$$

2.3.2.4 Back Face of Channel Receiver

The back face of the receiver is only exposed to high-temperature gas and the high-temperature piping that connects to the module cup. Hence, radiative emission and convective loss from that surface do not have large driving forces. And, since even that emitted radiation remains within the system, it is not counted as a loss. Therefore, for simplicity, the back face of the receiver is assumed to be thermally insulated and equations 19 and 20 apply.

2.3.2.5 Inflow Boundary Condition

The inlet boundary condition for the momentum equation is defined by setting an average velocity (U_0) normal to the surface. That can then be applied using the normal of the surface (**n**) as in equation 30 (COMSOL Multiphysics®, 2020a).

$$\mathbf{u} = -U_0 \mathbf{n} \quad (30)$$

For the energy equation at the same boundary, an energy balance at the surface can yield the following form of the Danckwert-type boundary condition:

$$k_g \nabla T_g \cdot \mathbf{n} = \rho_g \, \Delta H \, \mathbf{u} \cdot \mathbf{n} \quad (31)$$

Where ΔH is the mass-specific enthalpy difference between upstream and inlet conditions and is defined as the sum of enthalpy change due to temperature gradients and pressure gradients across the boundary, as in eqn. 32 below.

$$\Delta H = \int_{T_{upstream}}^{T_{in}} C_p \, dT + \int_{T_{upstream}}^{p_{in}} \frac{1}{\rho_g}\left(1 - \frac{\partial \ln \rho_g}{\partial \ln T_g}\right) dp \qquad 32$$

Where T_{in} & p_{in} ≡ inlet temperature and pressure, respectively

2.3.2.6 Outflow Boundary Condition

Defining the same property at both the flow inlet and outlet can end up over-constraining the problem. Hence, the outlet was described as reaching a normal stress on the boundary ($\hat{p}_0$) that includes viscous stress and the fluid pressure acting normal to the outlet surface. The total normal stress is set to atmospheric condition, so the summation leaves equation 33 in terms of gauge pressure. (COMSOL Multiphysics®, 2020a).

$$[-p\boldsymbol{I} + \boldsymbol{K}]\mathbf{n} = -\hat{p}_0\mathbf{n} \qquad 33$$

2.4 Implementation

2.4.1 General Solution Algorithm

There were two attempts made to simulate the transport equations previously described:

1. A finite differences implementation that was 3-dimensional in the solid domain and 1-dimensional in the fluid domain. It only solved the energy and radiative transport equations. All radiative transport (including external and mutual irradiance sources) was modeled using MCRT. The momentum equations were replaced by a convection boundary condition to reduce the computational load. This simulation was performed by a code written in Julia.
2. A finite element implementation that was 3-dimensional in both the solid and fluid phases. In it, only primary or external irradiance was modeled using MCRT. Mutual irradiance was modeled using the conventional direct integration approach.

2.4.2 1-D Finite Differences Simulation

To discretize this geometry in the $x-y$ plane, a semi-cylindrical coordinate system was used to create a boundary-fitted grid in the solid domain. The computational grid coordinates ζ, η, θ (or i, j, k in discrete form) range from 0 to 1 and are defined below and shown in Figure 2.8. Meanwhile, the gas phase was only discretized in the z-direction following the same intervals as the solid phase θ-discretization.

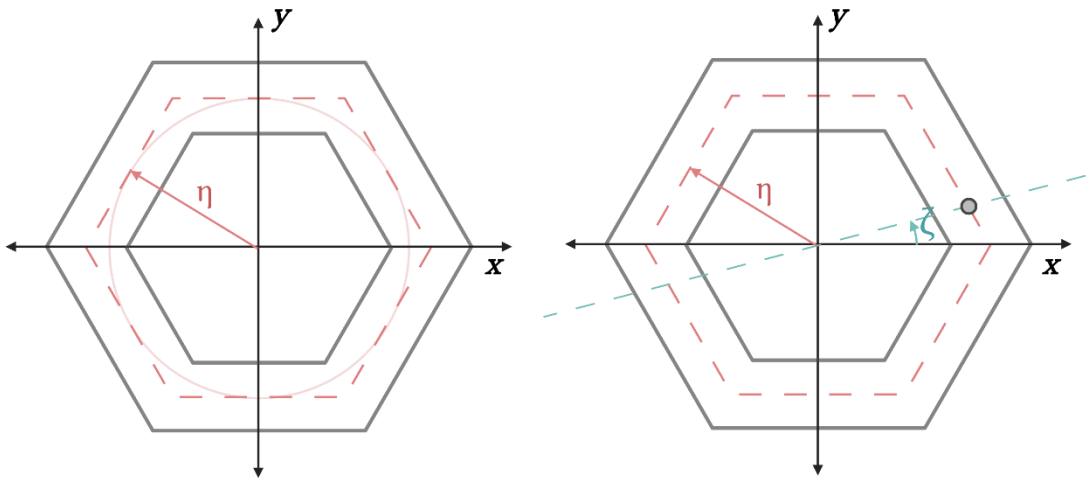

Figure 2.8: Computational domain coordinates used for FDM model

Where:

$\zeta \equiv$ a normalized angle off of the x-axis for a line going through the origin normal to the z-axis.

$\eta \equiv$ a normalized hexagon radius (here, hexagon radius is the radius of its inscribed circle).

$\theta \equiv$ a normalized z-axis measurement.

$$\zeta = \begin{cases} \frac{3}{\pi} * \tan^{-1}\left(\frac{y}{x}\right) - 1 & x > 0 \; and \; y \geq 0 \\ \frac{3}{\pi} * \left(\tan^{-1}\left(\frac{x}{y}\right) + \frac{\pi}{2}\right) - 1 & x \leq 0 \; and \; y > 0 \end{cases} \quad (34)$$

$$\eta = \frac{R - R_{min}}{R_{max} - R_{min}} \quad (35)$$

$$R = \sqrt{x^2 + y^2} \qquad 36$$

Where $R \equiv$ the radius of the hexagon intersecting the point (x, y) [m]

To use the developed boundary-fitted grid, the energy equation and its boundary conditions are transformed from cartesian coordinates to the computational domain coordinates to yield the derivative forms shown in equations 37 and 38.

$$\nabla^2 u = \frac{\partial^2 u}{\partial \zeta^2}\,(\nabla\zeta)^2 + \frac{\partial^2 u}{\partial \eta^2}(\nabla\eta)^2 + \frac{\partial^2 u}{\partial \theta^2}\,(\nabla\theta)^2 + 2\frac{\partial^2 u}{\partial \zeta\,\partial \eta}\,(\nabla\zeta \cdot \nabla\eta) \qquad 37$$

$$\nabla u = \frac{\partial u}{\partial \zeta}\,\nabla\zeta + \frac{\partial u}{\partial \eta}\,\nabla\eta + \frac{\partial u}{\partial \theta}\,\nabla\theta \qquad 38$$

Where 'u' is a name for any dependent variable and the direct transformation metrics ($\partial\zeta/\partial x\,, \partial\zeta/\partial y$, etc.) were estimated from the inverse transformation metrics ($\partial x/\partial\zeta\,, \partial y/\partial\zeta$, etc.) using a central difference scheme to avoid the singularities that come with directly differentiating $x(\zeta, \eta)$ and $y(\zeta, \eta)$.

Using this discretization, the energy equation for the gas phase can be derived using a macroscopic energy balance as shown in Figure 2.9 to yield equations 39 and 40 below. Since this equation is one dimensional in space, it only requires 2 boundary conditions: the inflow and outflow boundary conditions described in sections 2.3.2.5 and 2.3.2.6. Furthermore, calculating the heat transfer coefficient to evaluate the convective flux source term was done using a Nusselt number correlation given by (Turgut and Sarı, 2013) for turbulent flow in isothermal square and hexagonal ducts reproduced in eqn. 41 below.

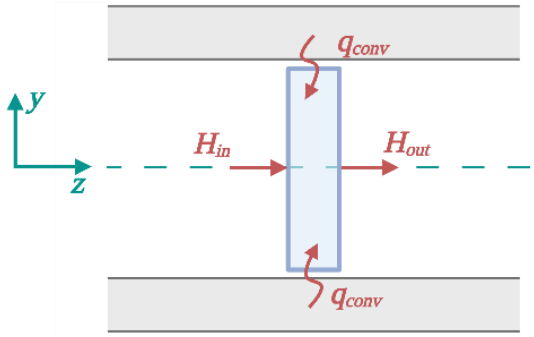

Figure 2.9: Discrete energy balance on the gas

$$\rho_g \, C_{p,g} \frac{\partial T_g}{\partial t} = \frac{\dot{m} \, C_{p,g}}{A_{cs}} \frac{\partial T_g}{\partial z} + \mathbf{q_{conv,f}} * \frac{1}{D_h} \tag{39}$$

$$\left.\frac{dT_g}{dt}\right|_k = \frac{\dot{m}}{\rho V_k}\left(T_g|_{(k-1)} - T_g|_{(k+1)}\right) + \frac{A_k}{\rho V_k \, C_{p,g}} \mathbf{q_{conv,f}}|_k \tag{40}$$

$$Nu = 0.023 * Re^{0.775}; \quad (2300 < \text{Re} < 52000) \tag{41}$$

$$h_{conv,f} = \frac{Nu * k_g}{D_h} \tag{42}$$

Where $D_h \equiv$ hydraulic diameter of channel [m]

$h_{conv,f} \equiv$ heat transfer coefficient for forced convection

The boundary conditions for the solid phase energy equation follow equations 21 and 22 described in section 2.3.2.2. However, MCRT was used to model both external and mutual irradiance. The calculations for those radiative fluxes are described below.

1. *Primary Ray Fluxes (External Irradiance)*

The total external irradiance on an absorbing element 'i' is the product of the number of primary rays absorbed by that element and their respective powers. The power of primary rays was assumed to be uniformly distributed and equation 12 (introduced in section 2.2.2 and reproduced here) applies.

$$I_{ext}|_i = n_{ab,i} * P_{p,ray} \quad 12$$

2. Secondary Ray Fluxes (Mutual Irradiance)

Mutual irradiance was calculated in analogous way (see eqn. 43), but the power of secondary rays depends on the temperature of their emitting source element 'j' according to the Stefan-Boltzmann law. Here, the power of secondary rays emitted by element 'j' was also assumed to be uniformly distributed to all rays emitted by that element.

$$I_m|_i = \sum_j n_{s,rays,i}|_j * P_{s,ray}|_j \quad 43$$

$$P_{s,ray}|_j = \frac{A_j\, \varepsilon\sigma\, T_j^4}{n_{sec,em,\,j}} \quad 44$$

Where $P_{s,ray}|_j \equiv$ power of a secondary ray emitted by element 'j'

$n_{s,rays,i}|_j \equiv$ number of secondary rays emitted by element 'j' and absorbed by element 'i'

$n_{sec,em,\,j} \equiv$ number of secondary rays emitted by element 'j'

$A_j \equiv$ the emitting area of surface element 'j'

Finally, after discretizing the domain-transformed energy equations and boundary conditions in space using a central difference scheme, a system of ODEs was obtained. This system of ODEs was solved using the LSODA algorithm – an algorithm that mostly uses an explicit scheme with adaptive time-stepping and switches to an implicit scheme when a stiff point is encountered – because it was the most efficient for stiff systems of equations larger than 2000 equations (Rackauckas and Nie, 2017).

2.4.3 3-D Finite Element Simulation

The finite element method (FEM) is based on the classical variational and weighted-residual methods, where the solution 'u' is represented as a linear combination of unknown parameters and appropriate approximation functions selected to satisfy the problem's boundary conditions. The key difference is that those methods apply the method to the entire domain of the problem (Ω), while FEM discretizes the system to subdomains (or elements) before selecting the approximation functions for each subdomain (Ω^e). This makes FEM more flexible to the complex geometries encountered in real-life systems. (Reddy and Gartling, 2010).

Typically, implementing the FEM requires the following steps:

1. Discretization of the problem domain (Ω) into subdomains (Ω^e) for which the same PDE applies.
2. Development of the weak form of the PDE and boundary conditions
3. Development of the finite element model
4. Assembly of finite elements to obtain a global system of algebraic equations
5. Imposition of boundary conditions
6. Solution of equations

However, the tool used (COMSOL Multiphysics®) only requires selecting the mesh properties and the physics models (transport equations) that need to be solved. Figure 2.10 below shows the physics and Multiphysics models used and the general way they are coupled.

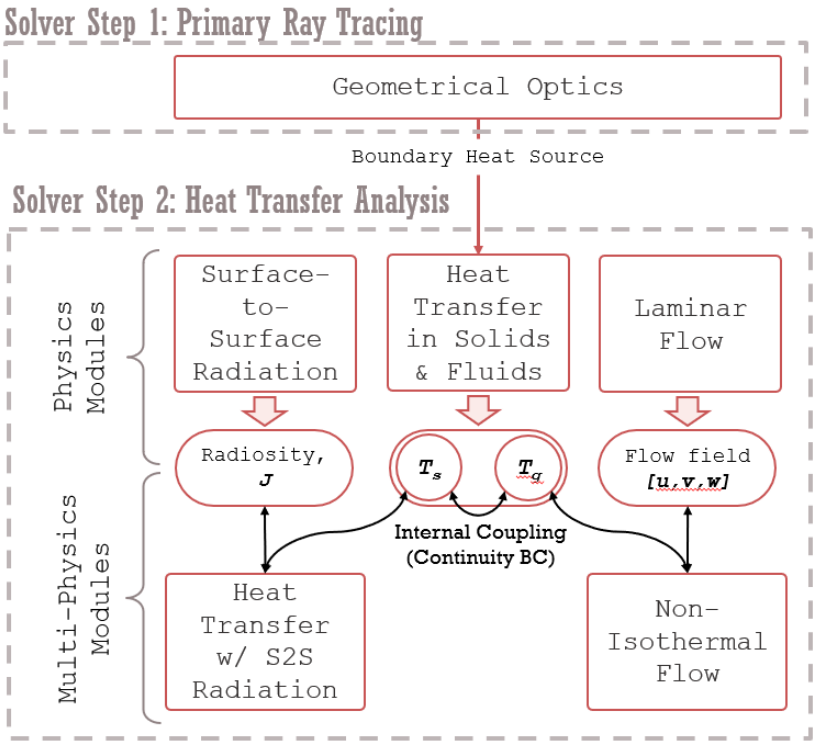

Figure 2.10: Structure of FEM model formulated using COMSOL

2.5 FDM Model Verification

2.5.1 Reference Case Description

Table 2.1 below lists the dimension parameters and operating conditions for the hexagonal channel used to verify the FDM model as described in the following sections.

Table 2.1: List of parameters used in verifying the developed FDM model

Parameter	***Value***
R_{ch}	2 mm
t_{ch}	0.25 mm
L_{ch}	100 mm
U_0	0.5 m/s
q'_{unif}	5 kW/m^2

2.5.2 MCRT Verification

To verify the MCRT results, the geometry and optical properties of the considered channel were recreated in the commercial MCRT software TracePro® with a given ray file for the source and the TracePro simulation results (absorption points) were exported to Julia. The same ray file was used to run the developed Julia MCRT code. A discrete absorption map in terms of the ray power absorbed by each element was created from both simulation results.

2.5.3 Heat Transfer Model Verification

The heat transfer model was verified by simulating a similar case in COMSOL. A uniform heat flux of 5 kW/m^2 was applied to the interior surfaces to mimic the flux applied by primary radiation, but without the stochastic effects that come with coarse or low-resolution MCRT. The front face of the channel was not heated and only exposed to natural convection. The gas properties were assumed independent of temperature and were averaged over the expected gas temperature range for the given uniform flux (i.e. 300K to 400K for dry air). The velocity field used for the reference FEM simulation was not solved for but was only specified at the entrance with the assumption of fully developed flow. The results of both models were compared qualitatively in terms of temperature profile and quantitatively using error in $T_s(z)$ and $T_g(z)$ in the final timestep.

2.5.4 Grid-Independence Study

To ensure the truncation error due to spatial discretization was acceptable and the solution was independent of the grid, a grid-independence study was performed using the same uniform-flux case used in section 2.5.3. The number of divisions in each direction ζ, η & θ was varied one at a time till the maximum temperature difference between two neighboring nodes was less than 0.01K.

Whenever the number of divisions in one dimension was varied, the number of divisions in the other two dimensions was left at 20 divisions.

2.6 FEM Model Verification

2.6.1 Reference Case Description

To verify the numerical model developed in COMSOL, the simulated temperature profile results for a reference case obtained from literature were replicated.

2.6.1.1 Receiver Geometry and Dimensions

The results replicated were the temperature profiles and performance charts of the HiTRec-II receiver geometry as simulated by (Capuano *et al.*, 2017). **Error! Reference source not found.** below lists the dimensions (channel radius (R_{ch}), length (L_{ch}) and wall thickness ($t_{ch} = t/2$)) of the HiTRec-II and the operating conditions used by the authors in the referenced work (the normal inflow velocity (U_0) and the radiative flux density on the receiver aperture (q'_{rad})). However, the boundary condition on the front wall was not clearly described, hence the natural convection coefficient 'h_{nat}' was assumed to be 5 W/m^{2}K, as that is the average for the typical range used in literature as mentioned in section 2.3.2.3.

Table 2.2: Dimensions and operating conditions for the verification system described by (Capuano et al.*, 2017)*

Dimensions	***Operating Conditions***	
$R_{ch} = 1mm$	$U_0 = 0.5\ m/s$	$T_0 = T_{amb} = 318\ K$
$L_{ch} = 50mm$	$q'_{rad} = 650\ kW/m^2$	$RH = 0.60$
$t/2 = 0.4\ mm$	$h_{nat} = 5\ W/m^2K$	-

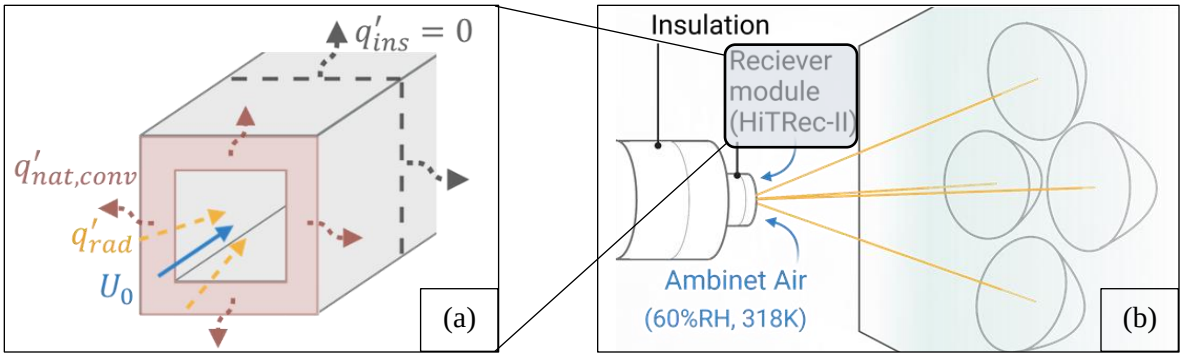

Figure 2.11: (a) Reduced system geometry and operating conditions (b) High flux solar simulator setup for the verification system described by (Capuano et al.*, 2017)*

2.6.1.2 Material Properties Used

The material of the receiver was siliconized silicon carbide (SiSiC), but the authors did not mention the thermal or optical properties used. Instead, thermal SiSiC properties published in (Munro, 1997) and reproduced in Table 2.3 below were used, and optical properties were varied to obtain the best fit to the published data. The properties of moist air with 60% relative humidity were also, used as ambient conditions.

Table 2.3: SiSiC thermal properties as published by (Munro, 1997)

Material Property	***Function***
Thermal conductivity, k_s	$52000 * \frac{e^{(-1.24*10^{-5}\,T)}}{(T+437)}$
Heat capacity, $C_{p,s}$	$1110 + 0.15\,T - 425 * e^{(-0.003\ T)}$
Density, ρ_s	$\rho(T) = \frac{3150}{[1+(T-300)\ \cdot (4.22 + 8.33 \times 10^{-4}T - 3.51e^{(-0.00527\,T)})]^3}$

Where T is the temperature in Kelvins.

2.6.1.3 Radiative Source Modelling

Furthermore, as the directional properties of the external radiation source are important, the external radiation source used in the reference case – the high flux solar simulator (HFSS) facility at the German Aerospace Center, aka DLR – was replicated. Only 4 concentrator modules (lamp,

parabolic reflector and cooling system) of the 10 available were employed (see Figure 2.12). The off-axis angle of the 4 reflectors were given by (Capuano *et al.*, 2017) and the reflector dimensions and properties were retrieved from (Alxneit and Dibowski, 2011). However, the position of the receiver with respect to the focal point was not given and the receiver face was assumed to be placed at the focal point of the HFSS.

Performing MCRT from the HFSS lamps all the way to the receiver channel in COMSOL every time would have been expensive and not necessary. Instead, primary rays were traced once from the HFSS lamps to a plane that is 5 mm in front of the receiver face. Then, the incident rays on that plane are stored in a ray file format (stores ray origin points, direction vectors and powers) and that file is used as the primary ray source in COMSOL. This step was performed using the commercial software TracePro, as reflector geometries are available as pre-defined parametrized objects, and ray tracing is more efficient because the surface equations for these pre-defined geometries are used as opposed to using the plane equations of discretized geometry elements. Finally, since only off-axis angles and power on aperture were provided, lamps were modelled as sphere with a surface release feature. And lamp powers were estimated using trial and error to achieve the desired power on aperture at the focal point. Table 2.4 below lists all the parameters used to generate the primary ray file.

Table 2.4: Reflector and lamp properties used in verification study

Reflector Properties *(Obtained from (Alxneit and Dibowski, 2011), unless otherwise stated)*	
Shape	Elliptical
Thickness (assumed)	1.4 [mm]
Hole radius	41 [mm]

Table 2.4: Reflector and lamp properties used in verification study (Continued)

Reflector Properties *(Obtained from (Alxneit and Dibowski, 2011), unless otherwise stated)*	
First focal length	80 [mm]
Second focal length	3000 [mm]
Diameter	775 [mm]
Length (calculated)	592.53 [mm]
Absolute position for x-z plane reflectors (calculated)	Origin = [534.8, 0, 3033.2] [mm] Rotation angle off each axis = [0°, 10°, 0°]
Absolute position for y-z plane reflectors (calculated)	Origin = [0, 1228.15, 2824.5] [mm] Rotation angle off each axis = [23.5°, 0°, 0°]
Lamp Surface Source Properties *(Determined by trial and error)*	
Emission type	Flux, radiometric units
Angular distribution	Lambertian
Flux	2300 [W]
Wavelength	500 [μm]
Number of rays released	10,000,000

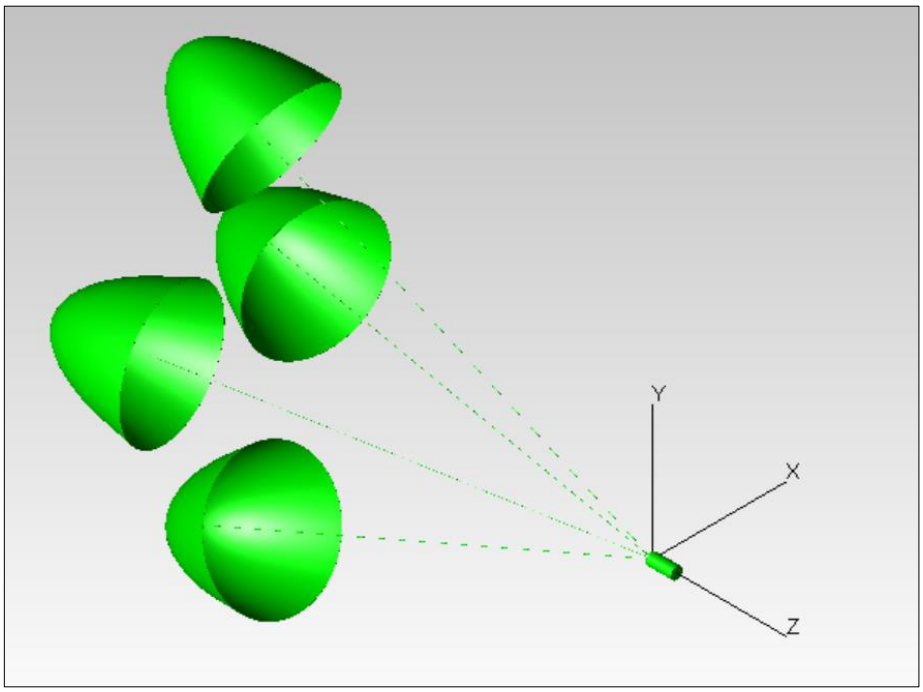

Figure 2.12: High flux solar simulator recreated from reference verification case

2.6.2 Grid-Independence Study

To select a mesh that ensures the accuracy of the implemented studies at a conservative simulation time, a grid-independence study was carried out. To achieve that, the mesh size was incrementally increased while tracking the change in the following global variables:

1. RMSE in $T_g(z)$ and $T_s(z)$ compared to the results published by (Capuano *et al.*, 2017) in the reference case described in section 2.6.1.
2. Response parameters, η_{th} and $T_{g,out}$.

The mesh was automatically generated by COMSOL, accounting for the different requirements of each included physics model and a user-specified element size level (e.g. coarse, normal, fine). Each mesh was constructed from tetrahedral elements that are uniform in size in the solid domain and grow from the walls to the bulk of the fluid domain. After the tetrahedral mesh is generated, 2 boundary layers with splitting corner treatment are added to resolve the high velocity gradients near the wall. Mesh size for the reference case described in section 2.6.1 was incremented along the default settings shown in Table 2.5.

Table 2.5: Predefined element size parameters used in COMSOL Multiphysics® (calibrated for fluid dynamics)

Element Size	**Maximum Size [mm]**	**Minimum Size [mm]**	**Growth Rate**	**Curvature Factor**	**Resolution of Narrow Regions**
Extremely Coarse	1.29	0.273	1.4	1	0.3
Extra Coarse	0.779	0.195	1.3	0.9	0.4
Coarser	0.506	0.156	1.25	0.8	0.5
Coarse	0.39	0.117	1.2	0.7	0.6
Normal	0.261	0.0779	1.15	0.6	0.7
Fine	0.206	0.039	1.13	0.5	0.8

Decreasing the element size beyond the "Normal" setting over-loaded the memory available. Instead, to observe if a plateau is achieved, an intermediate element size (between "Normal" and "Coarse") was specified according to the following parameters.

Table 2.6: User-defined element size parameters used for an "intermediate" size mesh

Location	Maximum Size [mm]	Minimum Size [mm]	Growth Rate	Curvature Factor	Resolution of Narrow Regions
Fluid Domain	0.33	0.1	1.18	0.7	0.6
Fluid Wall	0.24	0.06	1.13	0.5	0.8
General Size Node	5.03	0.905	1.5	0.6	0.5

2.7 Sensitivity Analysis & Optimization

2.7.1 Response Parameters

The following two response variables will be used to evaluate the performance of the receivers developed in this work:

1. Thermal efficiency, η_{th}

This is evaluated as the ratio of the power utilized (heat gained by the gas) to the radiative energy provided to the system (power on aperture, P_{ap}). However, since the power distribution of power on aperture is not uniform, the actual power that would be intercepted by a plane covering the front of the modelled receiver channel is used in place of the average flux density.

$$\eta_{th} = \frac{\dot{m}\, C_{p,g}\left(T_{g,out} - T_{g,in}\right)}{P_{ap}} \qquad 45$$

Where $T_{g,in}$ is the average inflow gas temperature.

2. Average gas outflow temperature, $T_{g,out}$

Since the exit gas temperature normally increases in the opposite direction to efficiency, it is important to find a region where improving thermal efficiency does not significantly impact the exit gas temperature.

$$T_{g,out} = \frac{\int_{A_{CS}} T_g(x, y, L_{ch}).\, dA_{CS}}{A_{CS}} \qquad 46$$

Where $A_{CS} \equiv$ the cross-sectional area of the channel [m^2]

3. Volumetric effect ratio, E_{vol}

The key thesis of this work is that varied reflectivity will induce the volumetric effect and in turn improve the thermal efficiency. However, there is no quantitative definition for the volumetric effect. In most works it is described by directly observing the temperature profiles, but that would not be feasible in the current work considering the number of simulations planned. Instead, volumetric effect will be quantified by the ratio of gas exit temperature and solid temperature at the inlet. This definition was used in recent works (Luque *et al.*, 2018).

$$E_{vol} = \frac{T_{g,out}}{T_{s,in}} \qquad 47$$

2.7.2 Fixed Parameters

1. Power on aperture to mass flowrate ratio ($P/\dot{m}$).

Fixing the $P/\dot{m}$ ratio ensures that all cases are compared under the same operating conditions. This was fixed at a value 700 J/kg, since this the value at which most works in literature report performance (see Table 1.1 for reference).

2. Module front area and dimensions (A_{mod}). The value for this was set at the same as that for the HiTRec-II as it is the basis of comparison in this work.

3. Radiative source characteristics (as described in section 2.6.1).
4. Channel thickness (t_{ch}).

Both channel radius and thickness affect porosity, which is a key design parameter. However, it is more meaningful to change porosity through changing channel radius instead of wall thickness since wall thickness is mostly selected based on structural integrity rather than thermal performance. Additionally, structural mechanics and the effects of thermal stress are not considered in this work, assuming that the material selected would be a ceramic known for stability in CSP applications. Hence, channel thickness is fixed at 0.5 mm (equivalent to a wall thickness of 1 mm), because that thickness is achievable in manufacturing and is similar to the wall thickness of the HiTRec-II.

5. Upstream or ambient gas properties (T_{amb}, RH_{amb}, p_{amb})

Table 2.7: List of fixed parameters used in sensitivity analysis

No.	***Fixed Parameter***	***Value***
1	*$P/\dot{m}$ ratio*	700 [J/kg]
2	*Module Dimensions*	Square, side length = 7 [cm]
3	*Radiative Source Characteristics*	
	Flux density, q'_{rad}	6.5×10^5 [W/m^2]
	Angle off x-axis	10°
	Angle off y-axis	23°
4	*Channel thickness, t_{ch}*	0.5 [mm]
5	*Ambient/Upstream Conditions*	
	Ambient Temperature, T_{amb}	318 [K]
	Ambient relative humidity, RH_{amb}	0.60
	Ambient pressure, p_{amb}	1.0×10^5 [Pa]

2.7.3 Variable Parameters & Ranges

After fixing the operating and ambient conditions, what remains are the channel dimension and shape parameters (R_{ch}, t_{ch} and L_{ch}) and the reflectivity distribution parameters. 2 reflectivity distributions will be considered:

1. An axial linear distribution as shown in Figure 2.13. Where the absorptivity of the channel starts low at 'α_{low}' at the inlet and starts increasing with 'z' from a depth 'L_e' which denotes the entry region length and gradually ramps at a slope 'm' to the high absorbance value 'α_{high}'. This distribution has 2 parameters (L_e and m). The low and high absorbance limits are selected based on the capabilities of high temperature coatings used in linear CSP applications (Yu *et al.*, 2021).
2. Discrete values of reflectivity on each wall as in Figure 2.13 below. This option was explored as it is favorable from a manufacturing point of view as it is easier to apply a uniform reflectivity to a wall as opposed to a specified graded distribution. This distribution, also, has 2 parameters: (α_x and α_y) which denote the absorptivity of the walls parallel to the x-axis and y-axis, respectively.

Ideally, all the reflectivity distribution parameters (L_e and m or α_x and α_y) and the channel size parameters (R_{ch}, t_{ch} and L_{ch}) could be studied simultaneously. However, because of the computational load that would require, the parametric study for each distribution was done in stages.

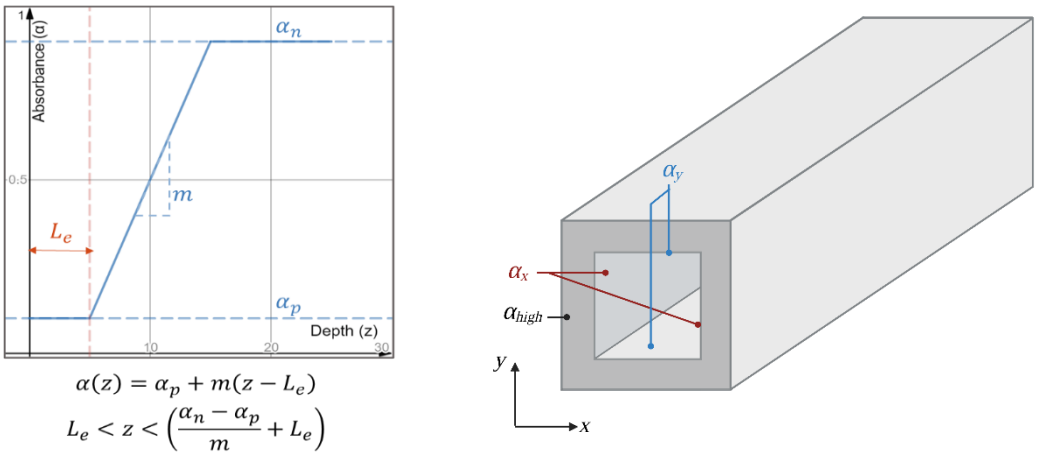

$$\alpha(z) = \alpha_p + m(z - L_e)$$

$$L_e < z < \left(\frac{\alpha_n - \alpha_p}{m} + L_e\right)$$

Figure 2.13: Reflectivity distributions considered. Right: Linear distribution, Left: Wall-varied distribution

2.7.3.1 Linear Distribution Parametric Study

In the first stage, only R_{ch} and L_e/L_{ch} are varied, because they were expected to have the greatest mutual effect in terms of radiation penetration. The slope of gradation 'm' is set to a very high value to remove its influence leaving a stepped distribution like the one in Figure 2.14. Channel length is determined by a constant length-to-diameter 'L_{ch}/D' ratio and is treated mainly as a parameter for convective heat transfer. This stage is supposed to produce a favorable range of values for L_e/L_{ch} and R_{ch}.

Table 2.8: List of variables and values for first stage of axial distribution studies (stepped distribution)

Variable	***Levels***
R_{ch} [mm]	[0.5, 1, 2, 4, 8]
L_e/L_{ch}	[0.001, 0.3, 0.5, 0.7, 0.9]
m [1/m]	1000
L_{ch}/D	25
α_{high}	0.9
α_{low}	0.1

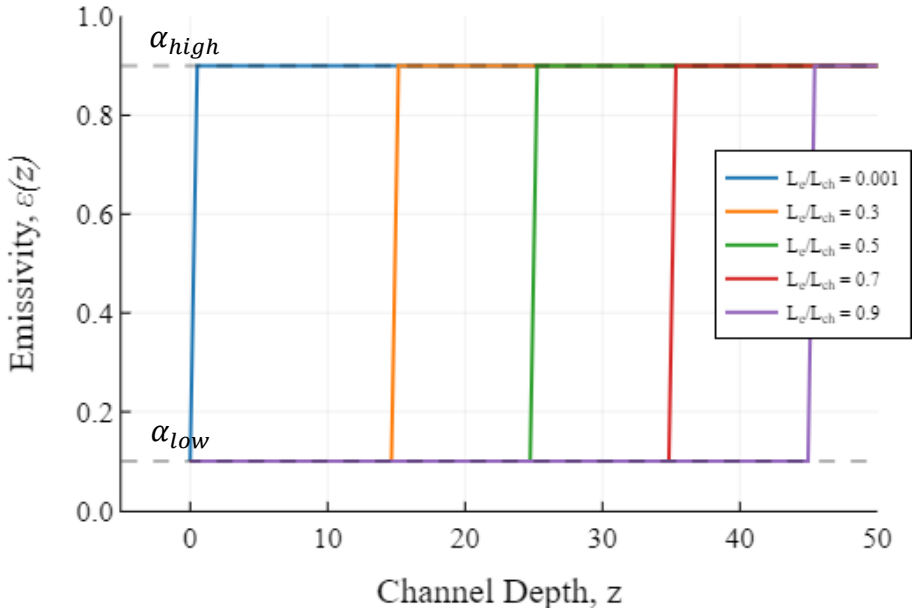

Figure 2.14: Stepped reflectivity distribution, ($\alpha(z)$ or $\varepsilon(z)$)

In the second stage, the channel length 'L_{ch}' and the slope of the distribution 'm' are optimized for with only two values of channel radii and one value for the reflective region length 'L_e/L_{ch}'.

Table 2.9: List of variables and values for second stage of axial distribution studies (graded distribution)

Variable	***Levels***
R_{ch} [mm]	0.5
L_e/L_{ch}	0.15
m [1/m]	$[10,\ 100, 1000]$
L_{ch}/D	$[10, 25, 50]$
α_{high}	0.9
α_{low}	0.1

2.7.3.2 Discrete Wall Reflectivity Parametric Study

First, R_{ch} and α_x are varied with α_y set at the high limit. Then, the inverse is done where α_x is fixed while R_{ch} and α_y are varied. This stage is meant to observe if incidence angle would have

any effect on the suggested receiver, considering that all walls are assumed to be purely diffuse. Channel length was treated the same way as it was in the linear distribution study, giving Table 2.10 for the study parameters. Channel length is optimized for in stage two, described in Table 2.11.

Table 2.10: List of variables and values for first stage of discrete wall reflectivity studies (exploring effect of off-axis angle)

Stage No.	***Variable***	***Levels***
1A	α_y	$[0.1, 0.3,\ 0.5,\ 0.7, 0.9]$
	R_{ch} [mm]	$[0.5, 1, 2, 4, 8]$
	L_{ch}/D	25
1B	α_x	$[0.1, 0.3,\ 0.5,\ 0.7, 0.9]$
	R_{ch} [mm]	$[0.5, 1, 2, 4, 8]$
	L_{ch}/D	25

Table 2.11: List of variables and values for second stage of discrete wall reflectivity studies (optimizing for channel length)

Variable	***Levels***
α_x	0.9
α_y	0.7
R_{ch} [mm]	0.5
L_{ch}/D	$[10, 25, 50]$

2.7.3.3 Base Case Parametric Study

The varied reflectivity receiver concept was compared to a receiver of uniform reflectivity whose size and emissivity were selected based on a similar parametric study to the ones described in sections 2.7.3.1 and 2.7.3.2. The variables and levels for each stage are summarized in Table 2.12 below.

Table 2.12: List of variables and values for the first and second stages of the base case receiver parametric study

Stage No.	***Variable***	***Levels***
1	α	$[0.3,\ 0.5,\ 0.7, 0.9]$
Optical	R_{ch} [mm]	$[0.5, 1, 2, 4, 8]$
Param.	L_{ch}/D	25
2	α	0.8
Heat Transfer	R_{ch} [mm]	1
Param.	L_{ch}/D	$[10, 25, 50]$

2.7.3.4 Additional Calculations

In any set of simulations where the radius is varied, the mass flowrate per module is maintained (to maintain the same $P/\dot{m}$ ratio) using the following equations:

The number of channels per row '$n_{ch,row}$' for a square receiver module is defined by eqn. 48, and the number of channels for the whole module 'n_{ch}' is the square of '$n_{ch,row}$'. Finally, the mass flowrate per channel is the mass flowrate per module uniformly distributed over 'n_{ch}'.

$$D_{tot} = n_{ch,row} * 2(R_{ch} + t_{ch}) \quad (48)$$

$$n_{ch} = \left(n_{ch,row}\right)^2 = \left(\frac{D_{tot}}{2(R_{ch} + t_{ch})}\right)^2 \quad (49)$$

$$\dot{m}_{ch} = \frac{\dot{m}_{mod}}{n_{ch}} \quad (50)$$

$$U_0 = \frac{\dot{m}_{ch}}{\rho_g\, A_{ch}} \quad (51)$$

3. Results

3.1 FDM Model Verification Results

3.1.1 MCRT Verification Results

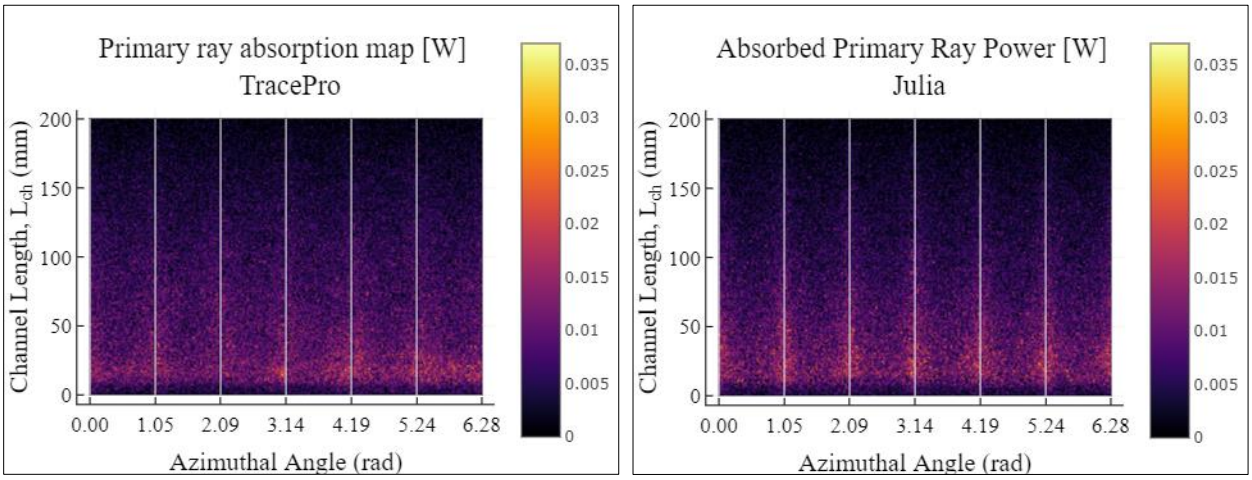

Figure 3.1 and Figure 3.2 show the results for MCRT verification (described in section 2.5.2).

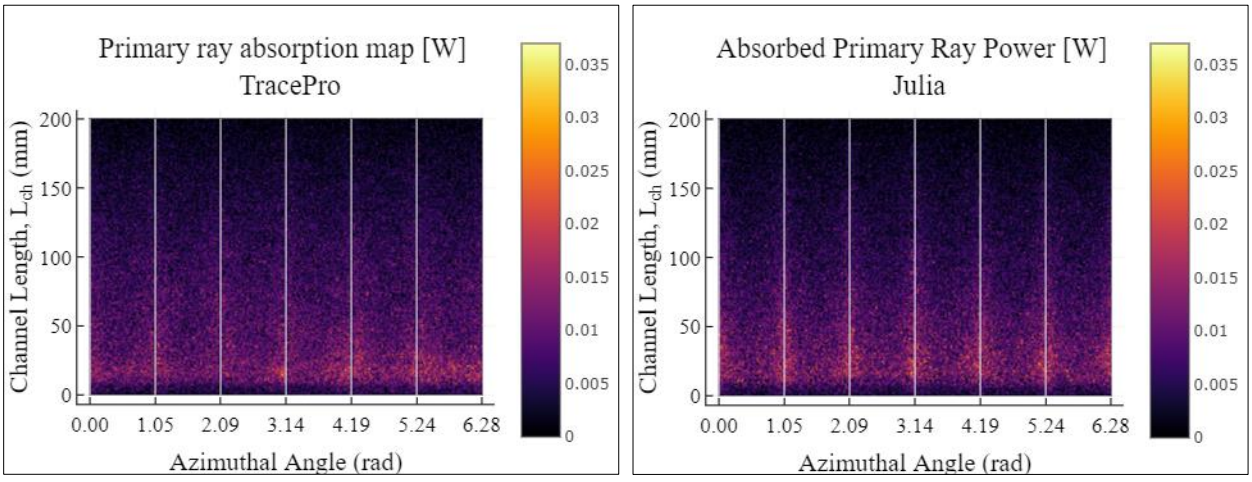

Figure 3.1 shows a slightly deeper penetration of rays in the TracePro results compared to the Julia results. This can be attributed to TracePro adding rays by interpolation. Because the number of rays defined by the source file was only around 18,000, while the number of rays absorbed by the channel was around 220,000 rays. To match this in Julia, the same source file was re-run multiple times to achieve a similar number of absorbed rays (about 215,000). Re-running with the same

rays is what could have caused the high local error at the front. Nevertheless, the average error is ≈ 0.0002 [W] which is less than 1% of the power range shown on the absorption maps in

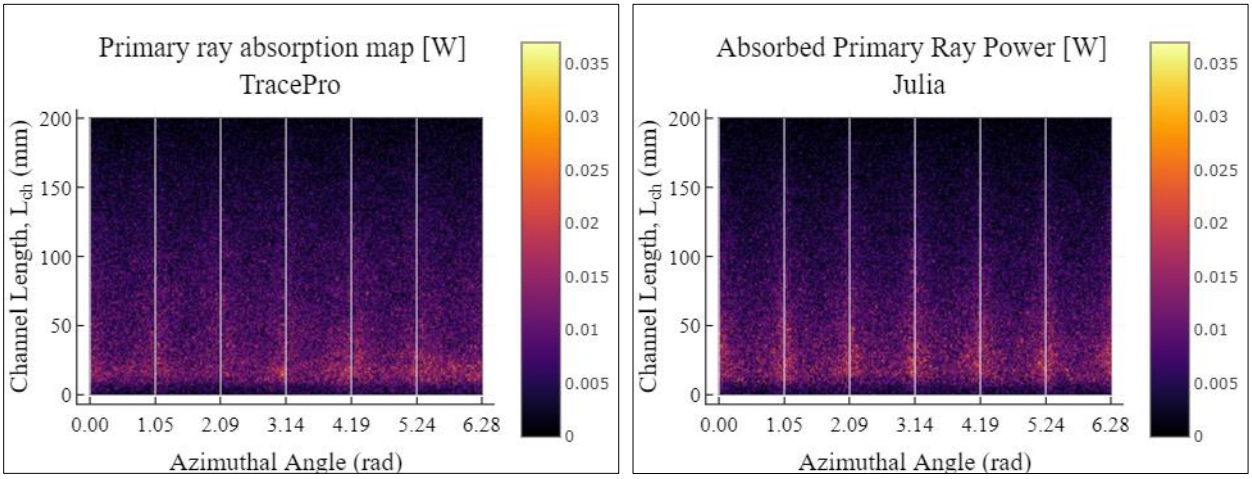

Figure 3.1.

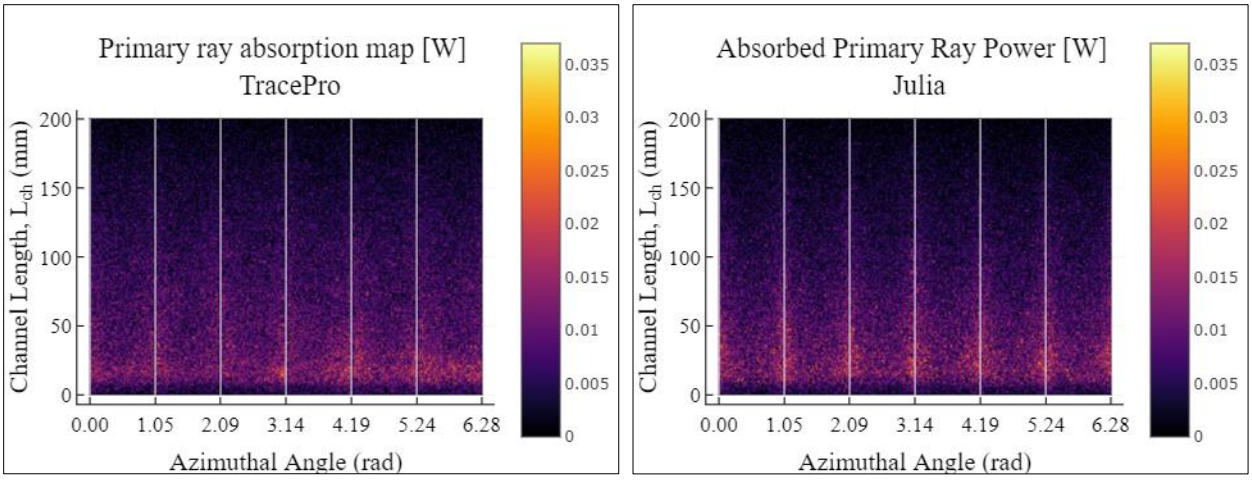

Figure 3.1: Primary ray absorption maps – Visual MCRT verification

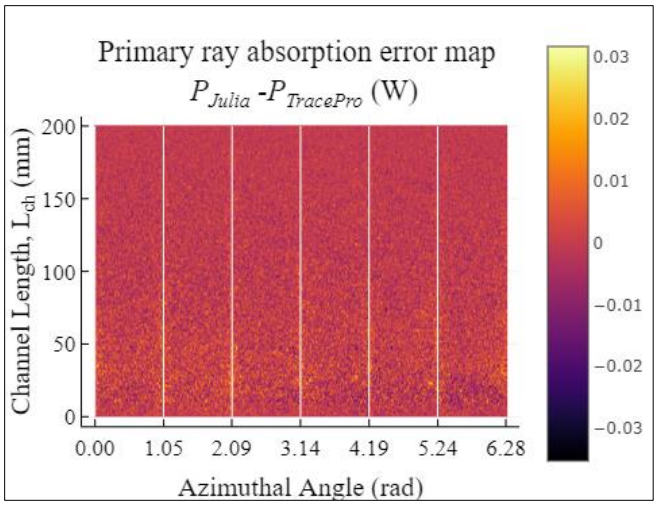

Figure 3.2: Primary ray absorption error map – Quantified MCRT Verification

3.1.2 Heat Transfer Model Verification Results

The first verification model developed in COMSOL (labelled COM1 in all subsequent text) solved the heat transfer in solids and fluids equation (eqn. 1) and showed a very large difference in behavior at steady state compared to the Julia FDM model – as shown in Figure 3.3. The gas temperature variation along the radial direction (or y-axis) is around 100K for COM1 and 0 K (as assumed) for the FDM model. The axial temperature distribution showed that COM1, also, exhibits a thermally developing flow whereas the Julia FDM model does not. Since the objective of the verification was to ensure that model equations were being implemented correctly, another heat transfer model was developed in COMSOL to remove the influence of formulation differences. This model was labelled COM2 and its assumptions are highlighted in Table 3.1 below.

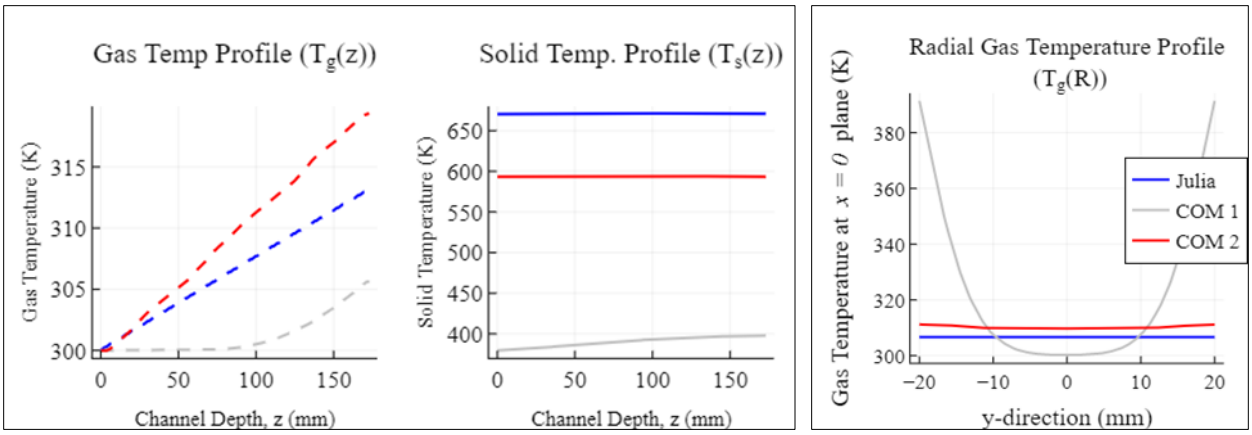

Figure 3.3: Comparing axial (left) and radial (right) temperature profiles of the 3 developed cases for a cavity receiver (Case A)

Table 3.1: Comparison between developed Julia and COMSOL verification models (COM1 and COM2)

Input Variations	***Model Name***		
	Julia	**COMSOL Sol. 1 (COM1)**	**COMSOL Sol. 2 (COM2)**
Gas velocity/ temp. profile	Flat – fully developed	Parabolic – developing	Parabolic – fully developed
Heat transfer coefficient	User-defined	Not needed	User-defined
Mesh for gas domain	No radial elements	Fine mesh in radial direction	Very few radial elements
Model physics	-	Heat Transfer in Solids and Fluids (coupled by no slip condition)	Heat Transfer in Solids Heat Transfer in Fluids (coupled through forced convection)

The second verification model (COM2) solved separate equations for heat transfer in solids and fluids (eqns. 2 & 4 respectively) and coupled them using a user-defined heat transfer coefficient. Additionally, to better approximate the flat temperature profile (or the single radial element) assumed by the FDM model, the mesh for COM2 was manually coarsened in the radial direction.

This produced a few low quality (highly skewed) elements, but the idea was that if a good agreement is obtained, then improving these approximations would be justified.

Employing the mentioned approximations, a better fit of behavior was obtained. Axial temperature profiles are of similar shapes, and only exhibit a shift in values. And the radial gas temperature profile is a closer approximation to the flat profile assumed in the Julia FDM model.

The plug flow assumption is more valid for higher Reynolds numbers, and the developed flow assumption is more valid for high length to diameter ratios. Thus, the issue became determining if these assumptions made to develop the FDM model were valid for the dimensions and operating ranges of a typical monolithic receiver. Table 3.2 lists the dimensions and conditions used in the first set of comparisons using the dimensions of a cavity receiver and the second set of comparisons that uses the dimensions of a typical monolithic volumetric receiver as described by (Ali *et al.*, 2020).

Table 3.2: Comparison of receiver dimensions and operating conditions used for FDM heat transfer model verification

Dimensions & Conditions	***Case A – Cavity Receiver***	***Case B – Monolithic Receiver***
R_{ch} [mm]	20	2
L_{ch} [mm]	172.9	100
t_{ch} [mm]	2.5	0.25
U_0 [m/s]	0.120	0.5
Source	(Sarwar *et al.*, 2015)	(Ali *et al.*, 2020)

Figure 3.4 below shows the results for Case B. The axial temperature profiles show that the developing flow and developed flow solutions exhibit the same behavior, indicating that the developed flow assumption is acceptable. However, the FDM results are far from both COMSOL solutions. This can be attributed to a significant radial temperature variation that is not accounted

for in the FDM model. Hence, using the FDM model for systems that operate in the ranges typical to volumetric honeycomb receivers would require incorporating momentum transport equations. This would have been difficult because of the added computational load and the steep learning curve associated with CFD modelling. Instead, time was invested in exploring the graded reflectivity receiver concept using COMSOL.

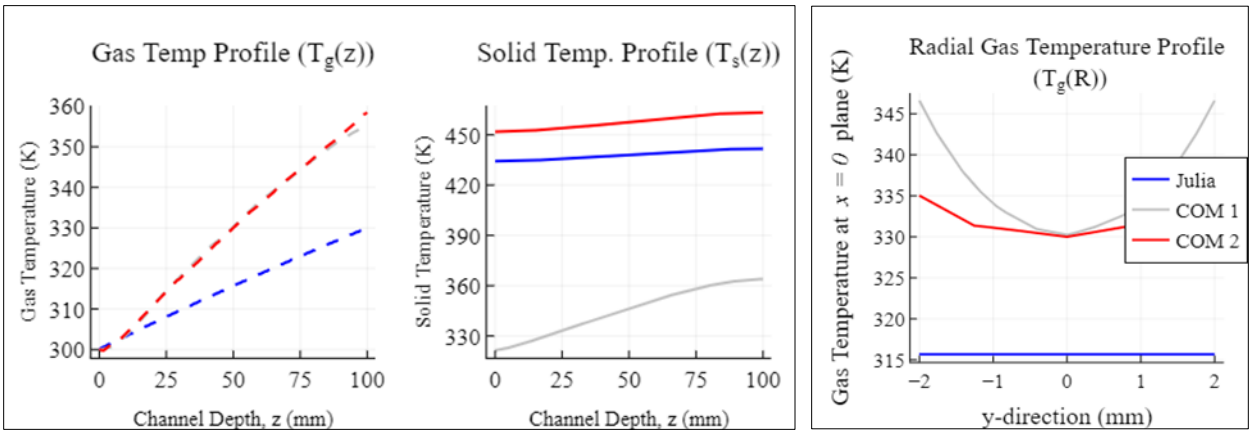

Figure 3.4: Comparing axial (left) and radial (right) temperature profiles of the 3 developed cases for a monolithic receiver (Case B)

3.1.3 Grid Independence Study Results

Figure 3.5 below shows the results for the grid-independence study described in section 2.5.4. The results below show that a grid of $\zeta \times \eta \times \theta = 10 \times 8 \times 200$ (or minimum dimensions: $[\Delta x,\ \Delta y,\ \Delta z] > [2.31,\ 0.25,\ 0.84]$ mm) is sufficient for the dimensions considered ($R_{ch} = 20$ mm, $L_{ch} = 170$ mm, $t_{ch} = 2.5$ mm).

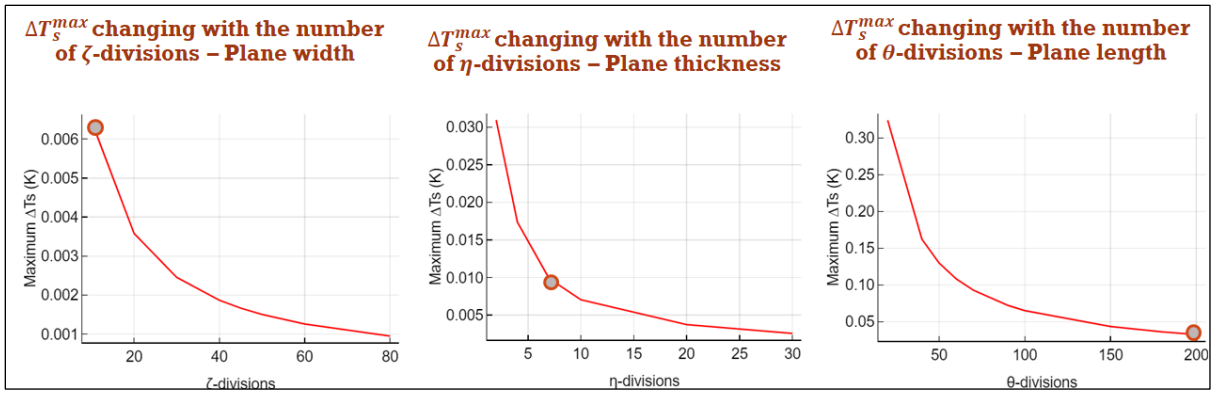

Figure 3.5: Grid-independence study for one set of channel dimensions

3.2 FEM Model Verification Results

3.2.1 Heat Transfer Verification Results

Figure 3.6 below shows the temperature profiles obtained in literature and in this work for the HiTRec-II receiver described in section 2.6.1. The gas temperature profile is very similar to the one presented in literature (error past 10mm is almost a straight line), but the deviation in gas exit temperature is nearly 200K. The solid temperature profile shows a less dramatic gradient at the inlet and a lower temperature change from inlet to outlet compared to the literature data (120K compared to 220K in literature). It, also, exhibits a fairly consistent local deviation of around 200K. Nevertheless, both in literature and in the current work, equilibrium ($T_g(z) = T_s(z)$) is reached at $z = 30$mm. These deviations in behavior (shape) and values can be attributed to uncertainties in the solid material properties used (k_s, $C_{p,s}$ and ε_s) and the gas inlet conditions provided in the literature.

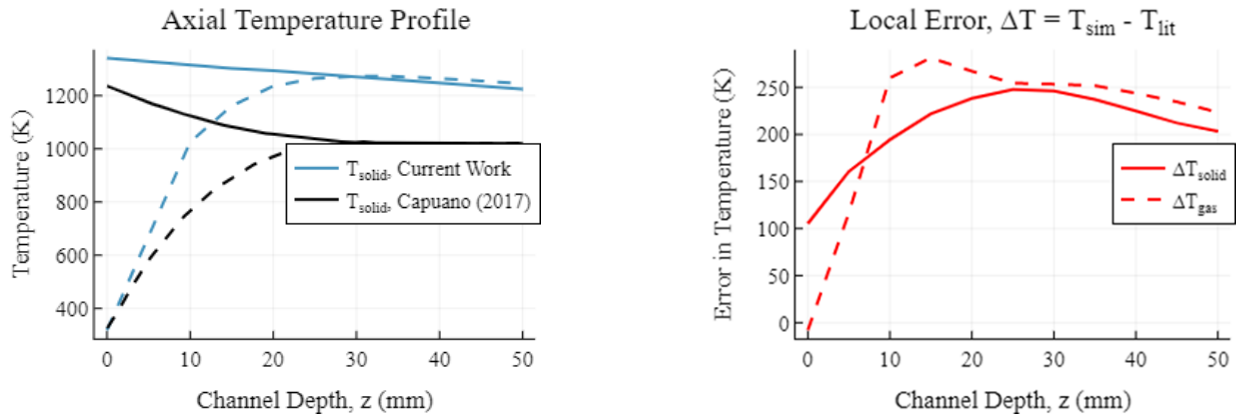

Figure 3.6: Verification results for FEM model – Left: axial temperature profiles; Right: deviation from literature in axial temperature profiles

The flatter solid temperature profile obtained in the current work, despite the majority of radiation being absorbed by the front face of the receiver (see Figure 3.7), implies a higher solid conductivity. As (Kribus *et al.*, 2014) showed that higher solid temperature gradients are observed for cases with low thermal conductivity (< 3 W/m·K), as opposed to the average SiSiC conductivity of 60 W/m·K used in the presented simulations. Figure 3.8 shows the effect of thermal conductivity on temperature profile. The higher solid temperature gradient for $k_s = 0.1$ W/m·K closely resembles the results presented by (Kribus *et al.*, 2014) (not shown here), while the very flat solid temperature profile at $k_s = 100$ W/m·K resembles the solid temperature profile obtained in this work.

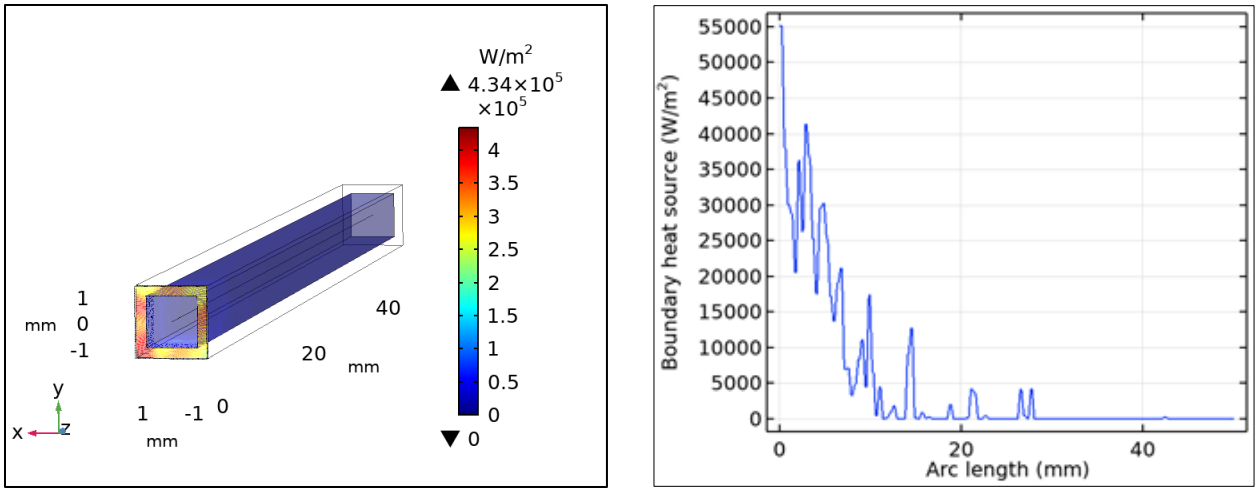

Figure 3.7: Boundary heat source (density of absorbed radiative flux) – Right: On a 3-dimensional geometry, and Left: along the receiver depth

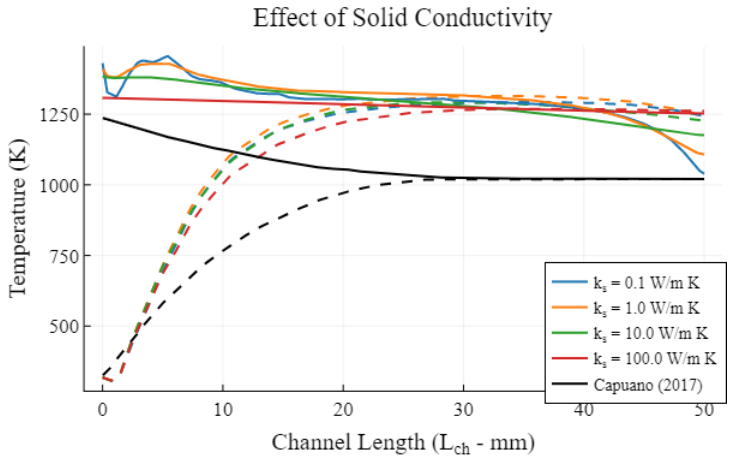

Figure 3.8: Effect of varying solid thermal conductivity on axial temperature profile

Furthermore, the surface emissivity and absorptivity used in literature were not explicitly provided. The results in Figure 3.6 assume a surface emissivity of 0.5. to test the influence of this assumption, the emissivity was varied between 0.5 and 0.8 and the results for that are in Figure 3.9 below. The figure shows that varying emissivity has a marked effect on the extent of deviation, but not on the temperature profile.

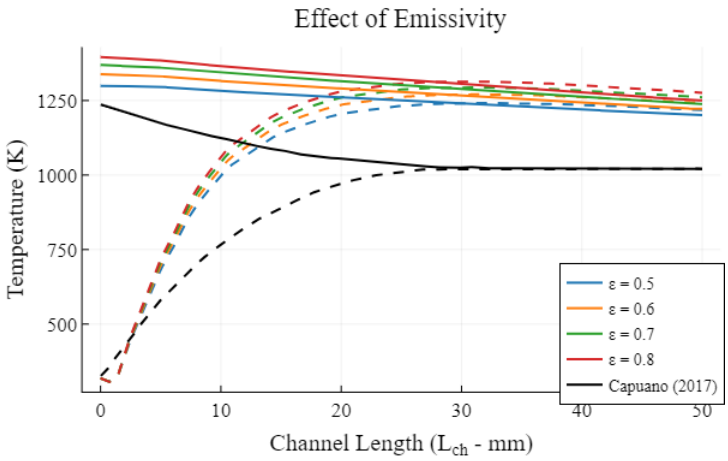

Figure 3.9: Effect of varying emissivity on axial temperature profile

A similar test was conducted to inlet gas velocity, since the velocity and mass flowrates provided in literature do not match for the given channel dimensions ($U_0 = 0.5$ m/s, $\dot{m} = 6 \times 10^{-6}$ kg/s for $A_{cs} = 4 \times 10^{-6}$ m^2). The figure below shows that a higher velocity significantly improves agreement with the solid temperature profile and exit gas temperatures, but none of the tested levels for velocity achieved a 1:1 agreement. Thus, deviations in temperature profile can be attributed to a combination of uncertainties in the solid thermal properties and the gas inlet conditions used to generate the literautre data.

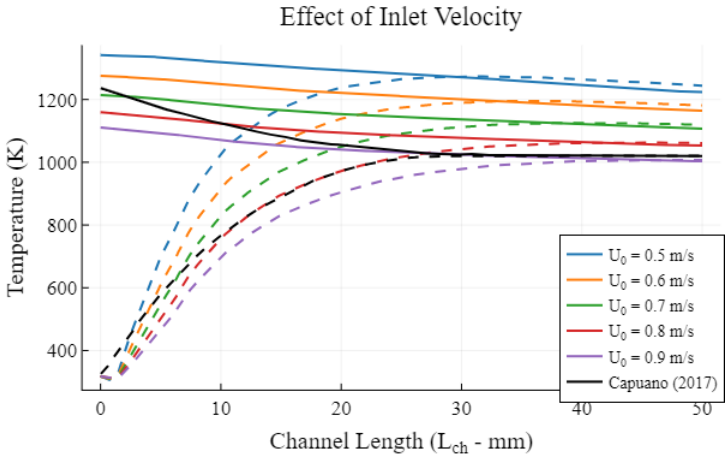

Figure 3.10: Effect of varying inlet gas velocity on axial temperature profile

3.2.2 Grid Independence Study Results

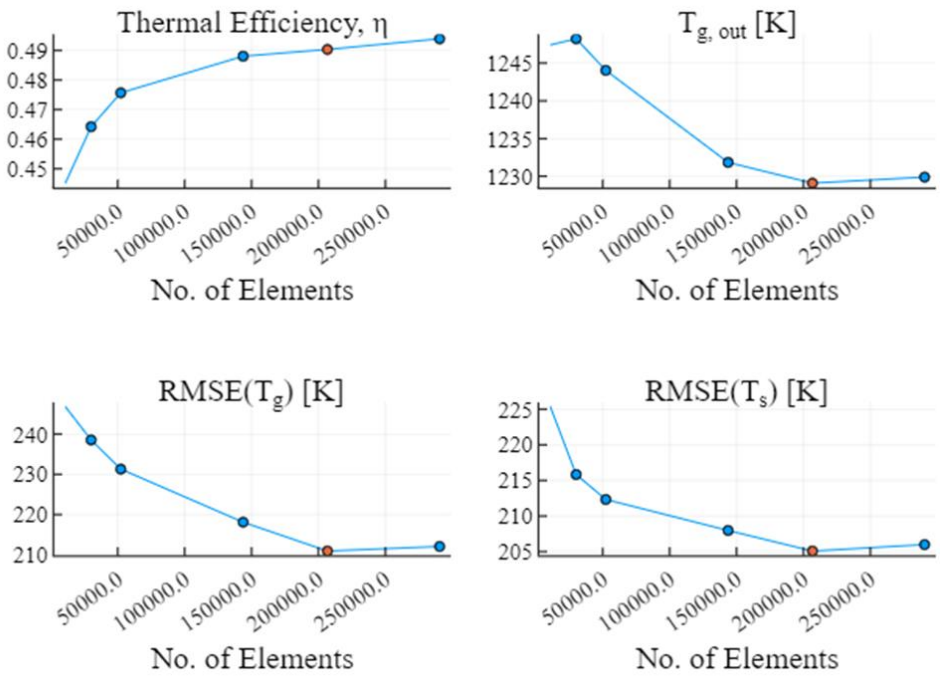

Figure 3.11: Mesh independence study results for FEM implementation

Each marked point on the plots in Figure 3.11 above corresponds to a size setting pre-defined in COMSOL Multi-physics, except for the points marked in orange – those correspond to the intermediate size mesh described in Table 2.6.

The plots in Figure 3.11 show that a plateau is reached when the mesh size is "Coarse", as doubling the number of mesh elements from 150k changes the efficiency by less than 0.01 and changes the other temperature indicators by less than 5K. However, considering that the simulation time of the "Coarse" mesh for a larger channel size would increase parabolically (see **Error! Reference source not found.**), it would not be economical to conduct the sensitivity analysis with that mesh size. Instead, all the sensitivity analysis results presented further in this work will be using a "Coarser" mesh as its simulation time scales at an acceptable rate and it does not over-estimate the relevant response variables (η and $T_{g,out}$).

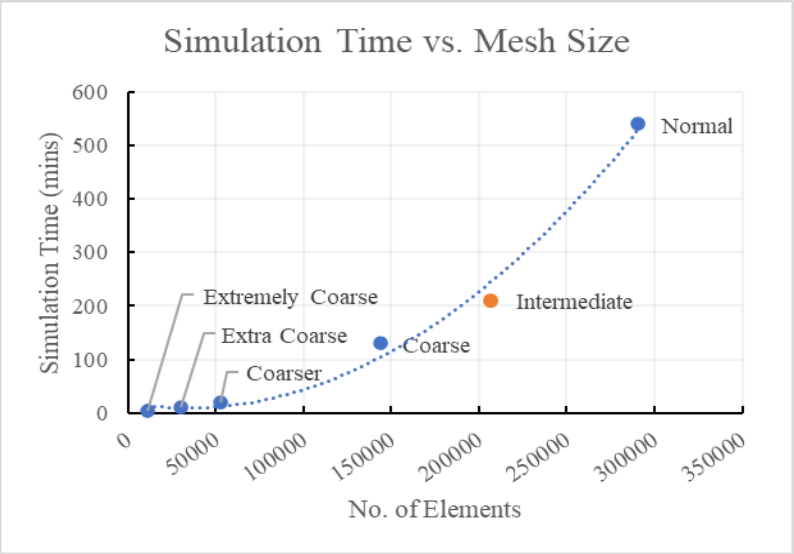

Figure 3.12: Simulation time vs. mesh size (for a Windows PC with 32GB RAM and 3.2GHz CPU)

3.3 Sensitivity Analysis Results

3.3.1 Base case

3.3.1.1 Stage 1 – Effect of Porosity and Emissivity

Figure 3.13 shows the thermal efficiency, exit gas temperature and volumetric effect ratio contours for the uniform reflectance base case described in section 2.7.3.3. Both exit gas temperature and efficiency increase with emissivity and exhibit a minimum with porosity or cell radius, while the volumetric effect ratio does not. This contradicts the expected dependencies where the maximum efficiency tends towards the highest porosity and lowest emissivity as that would minimize re-radiative losses. The maximum gas temperature should follow the highest emissivity and lowest porosity. Additionally, the volumetric effect is expected to increase for cases with high porosity and low emissivity as that reduces the frontal surface area and the solid temperature, but the opposite relationship with porosity is observed. Hence, a more thorough examination of the phenomena involved is needed.

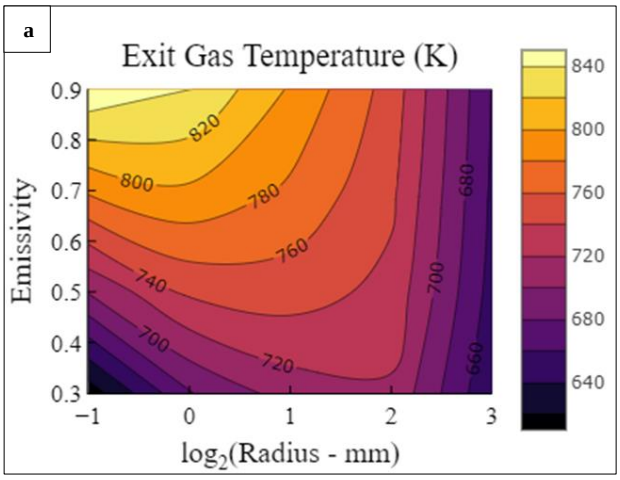

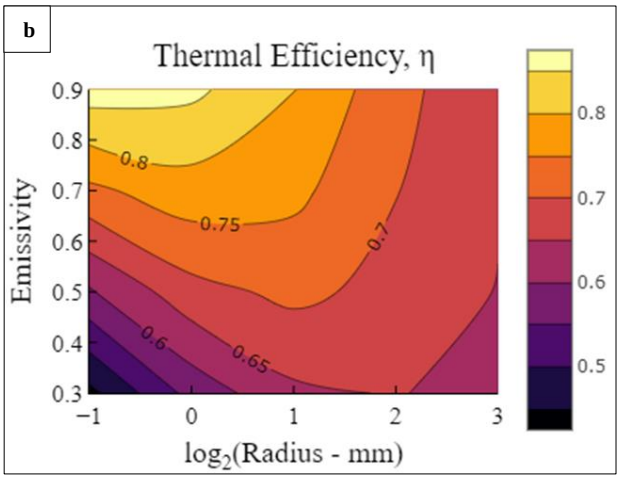

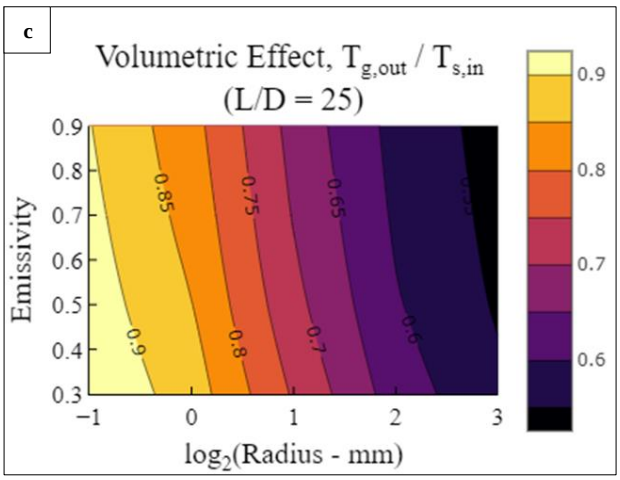

Plotted Independent Parameter	*Corresponding Independent Parameters*			
$\log_2(R_{ch})$	R_{ch} [mm]	ϕ	Re	Δp [Pa]
-1	0.5	0.309	32.4	42.90
0	1	0.510	39.2	13.70
1	2	0.694	57.6	5.50
2	4	0.826	96.8	2.68
3	8	0.907	176.4	1.46

Figure 3.13: Base case parametric study – results for effect of emissivity and porosity

Though porosity and pore size have been reported in previous works (Kribus *et al.*, 2014) to have a mutual effect on efficiency, the effect of changing pore radius on efficiency at a constant porosity reported in literature is very minimal (an increase of < 0.01). Hence, the following analysis will consider porosity and emissivity the key independent parameters.

Heat flows directly influencing thermal efficiency can be summarized as in the block diagram below. The energy streams shown in the diagram represent their sources and relative magnitude using color and thickness, respectively. Also, secondary and primary ray fluxes are indicated by the letters (S) and (P), respectively.

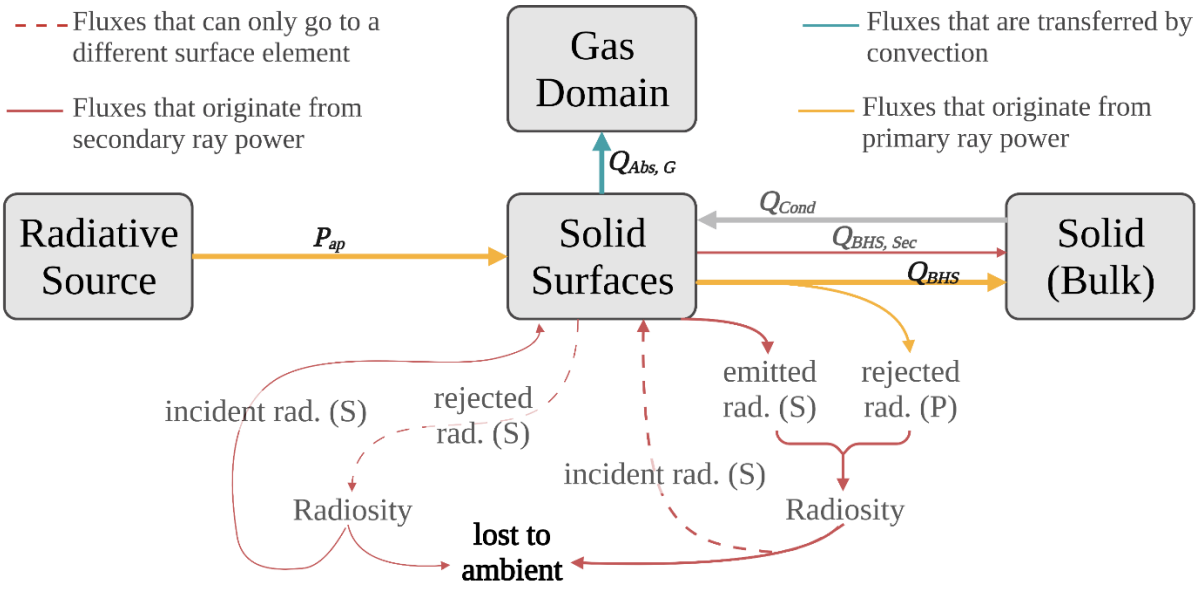

Figure 3.14: Breakdown of significant contributing energy streams in a volumetric air receiver

The power on aperture (P_{ap}), sensible heat absorbed by the gas ($Q_{abs,g}$), and the radiative loss to the ambient environment ($Q_{rad,loss}$) are highlighted as they are the key energy sources and sinks in the system. The primary radiative energy absorbed by the irradiated surfaces (or the boundary heat source, Q_{BHS}) is, also, highlighted as it is the largest intermediate energy flux compared to all the other secondary ray fluxes. The relationship between these energy streams and the independent variables will be studied to analyze the trend observed in Figure 3.13. However, since evaluations of these energy streams were based on a single channel, the collected values need to be normalized to the scale of a module. Because of this, power on aperture will be excluded since it will be the same for all cases when normalized. The other three parameters will be normalized as follows:

1. The total boundary heat source per channel (Q_{BHS}) is an integral over all participating surfaces and is normalized by dividing by the total area of the participating surfaces per channel. Increasing Q_{BHS} increases efficiency as it indicates a greater portion of the power on aperture is available to be transferred to the working fluid.

$$Q_{BHS} = n_{channels} * \int_{A_{rad}} Q_{BHS,ch}.dA_{rad} \quad 52$$

Where A_{rad} ≡ the area of all radiatively participating surfaces [m^2]

$n_{channels}$ ≡ the number of channels per module [-]

2. The sensible heat absorbed by the gas per channel ($Q_{abs,g}$) is normalized by multiplying by the number of channels. Increasing $Q_{abs,g}$ increases efficiency, by definition (see eqn. 45 for the definition of solar-to-thermal efficiency).

$$Q_{abs,g} = n_{channels} * \dot{m}_g \, C_{p,g}\left(\overline{T_{g,out}} - \overline{T_{g,in}}\right) \quad 53$$

3. The radiative loss will be evaluated using the surface average temperature for all elements with an ambient view factor greater than 0.01. This corresponds to an entry region that varies from 1% to 18% of the channel length as Figure 3.15 shows.

$$Q_{rad,loss} = n_{channels} * \int_{A_i} F_{amb,i} * \varepsilon \, \sigma \left(\overline{T_{s,i}}^4 - T_{amb}^4\right).dA_i \quad 54$$

Where subscript 'i' refers to all surface elements that satisfy the ambient view factor requirement mentioned above.

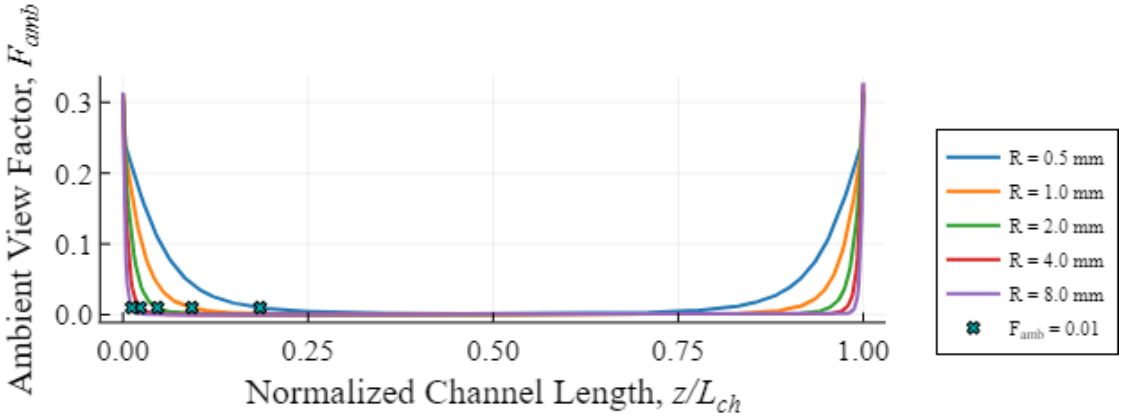

Figure 3.15: Ambient view factors for channel sizes considered in the base case

Figure 3.16 below shows how the relevant energy streams mentioned change with porosity and emissivity.

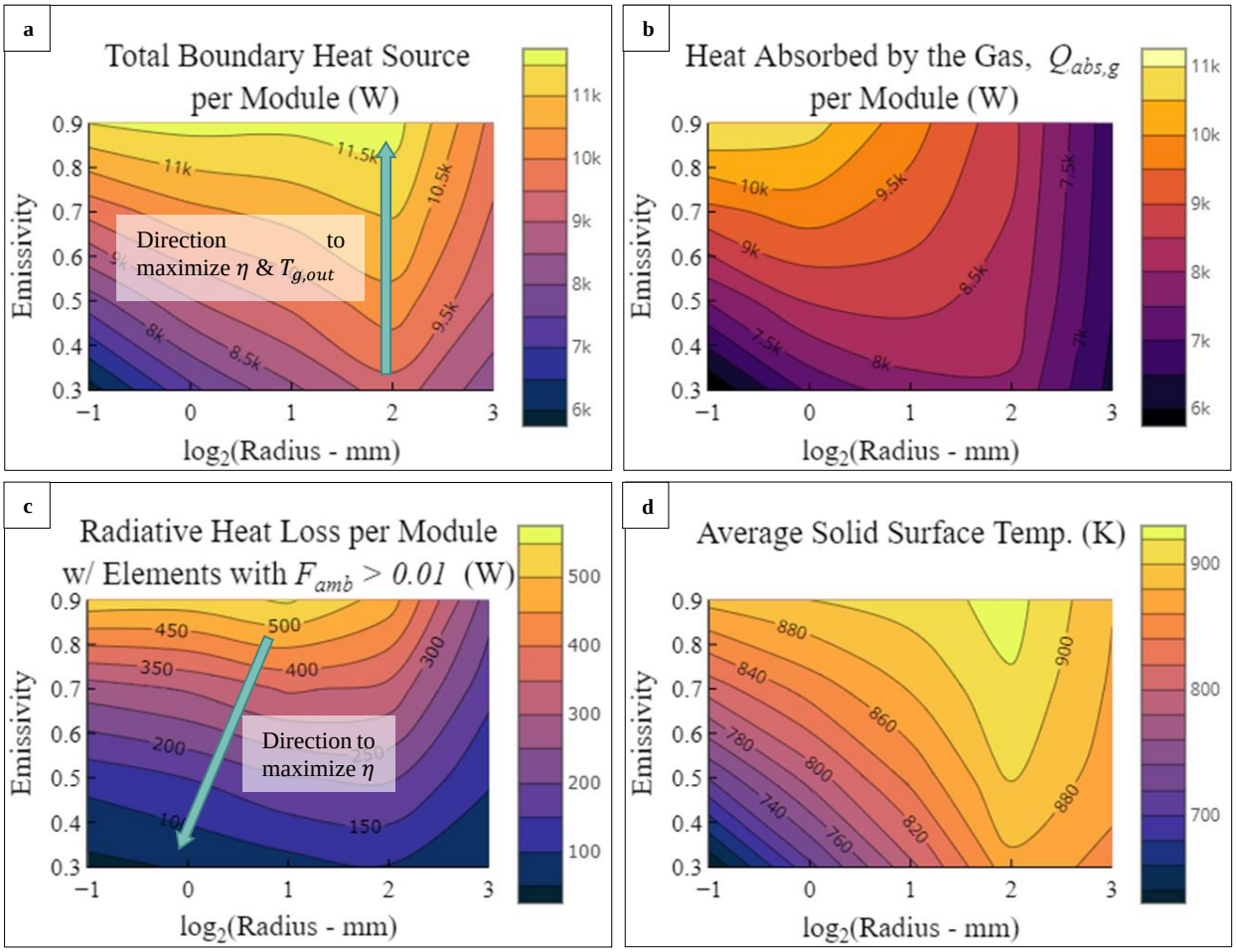

Figure 3.16: Analysis of key contributing energy streams for the base case – effect of ϕ and ε

It shows the heat absorbed by the gas following the same trend as the thermal efficiency, since efficiency is just $Q_{abs,g}$ divided by a constant power on aperture. More interestingly, the boundary heat source exhibits a strong maximum at $\log_2(R) = 2$. Unlike thermal efficiency, this maximum does not appear to be related to the emissivity. This maximum with porosity can be explained as a design that maximizes radiation penetration, while maintaining a large irradiated surface area. A corresponding maximum is seen in the plot for average solid surface temperature. Additionally, radiative heat loss is much smaller compared to the other fluxes considered. Nevertheless, it

increases with emissivity. And increases with porosity as solid temperature increases (for $\log_2(R) < 2$), then decreases as the frontal surface area decreases (for $\log_2(R) > 2$). The maximum with porosity observed in the plot for exit gas temperature can, therefore, be attributed to the boundary heat source and the total radiative loss. the direction that maximum efficiency follows, can be seen as the vector sum of the directions that maximize efficiency for radiative loss and boundary heat source (see the two blue arrows in Figure 3.16).

The trend observed for volumetric effect can be explained by Figure 3.17 below, which shows the inlet solid and the exit gas temperatures and the directions that would maximize volumetric effect. The trends for $T_{s,in}$ and $T_{g,out}$ were explained previously, and the direction that maximizes volumetric effect is, approximately, a weighted vector sum of the arrows shown in Figure 3.17.

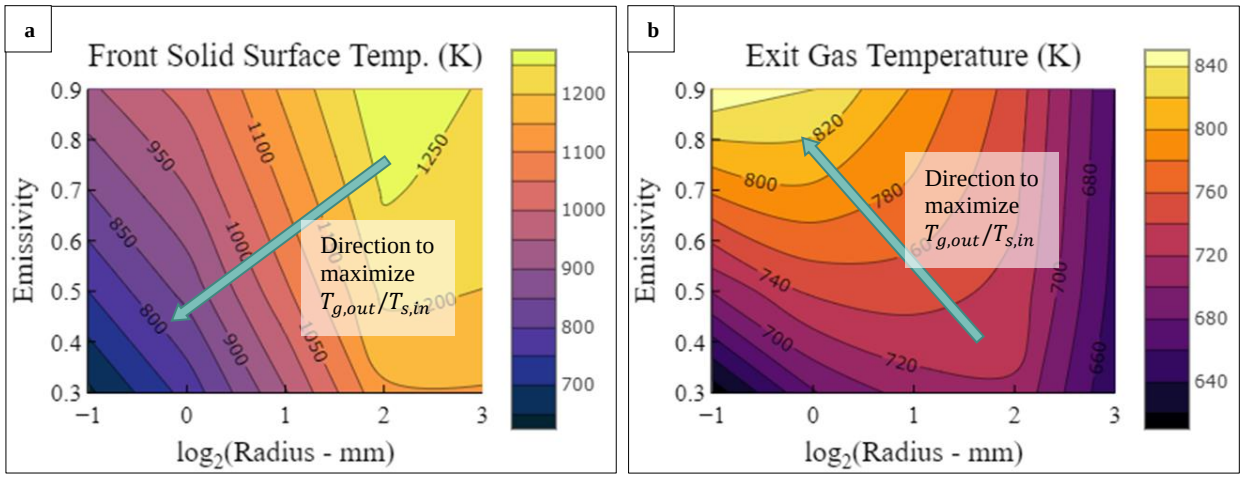

Figure 3.17: Analysis of components of volumetric effect – base case, effect of ϕ and ε

To optimize for channel length, the best performing combination of porosity and emissivity should be selected, which is $R_{ch} = 0.5[\text{mm}]$ and $\varepsilon = 0.9$. However, that would not allow comparison to the varied reflectivity receivers, since all the parametric studies of those receivers converge to the base case at the highest average emissivity. Hence, the optimal base case receiver at a lower

emissivity is selected for the second stage of length optimization and its parameters and performance are presented in Table 3.3 below.

Table 3.3: Optimized base case receiver after first stage ($L/D\ ratio\ =\ 25$)

Parameters & Responses	**Base Case Receiver**
Optimum design parameters	$(\varepsilon, R_{ch}) = (0.8, 1\text{mm})$
Exit gas temperature	820 K
Thermal efficiency	0.82
Volumetric effect ratio	0.85

3.3.1.2 Stage 2 – Effect of Channel Length

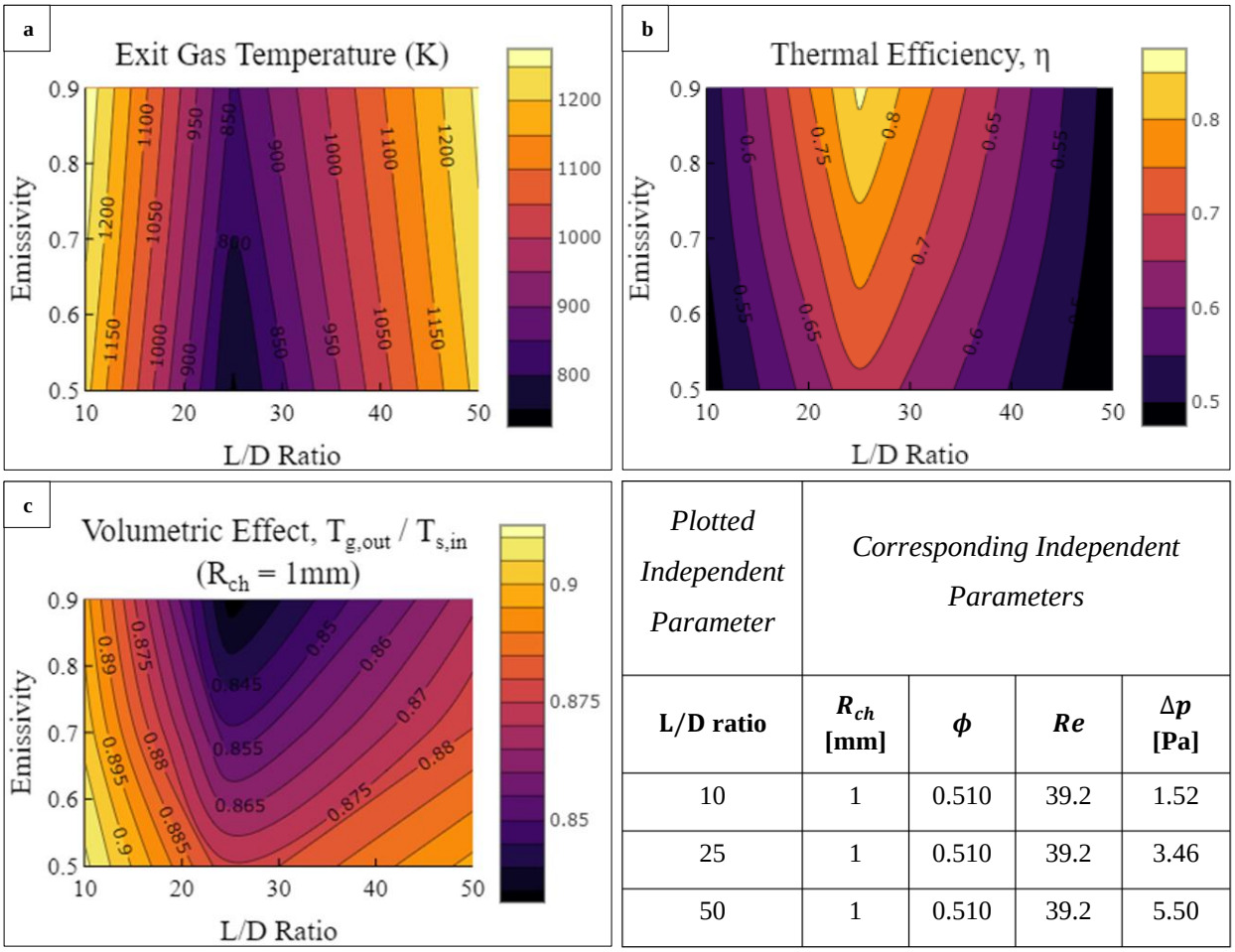

Plotted Independent Parameter	*Corresponding Independent Parameters*			
L/D ratio	**R_{ch} [mm]**	**ϕ**	**Re**	**Δp [Pa]**
10	1	0.510	39.2	1.52
25	1	0.510	39.2	3.46
50	1	0.510	39.2	5.50

Figure 3.18: Base case parametric study – results for effect of channel length

The larger picture with multiple channel lengths in Figure 3.18 shows that there is a length that maximizes thermal efficiency but minimizes volumetric effect and exit gas temperature. The maximum with efficiency can be attributed to maximized convective transport, as the plot for Q_{abs} in Figure 3.19 (b) exhibits a similar maximum, and channel length seems to have little to no effect on the boundary heat source in the selected range (see Figure 3.19 (a)). This implies most of the primary radiation is absorbed in a channel length less than 10 times the diameter. This, also, confirms that channel length is mostly a heat transfer parameter, not an optical one.

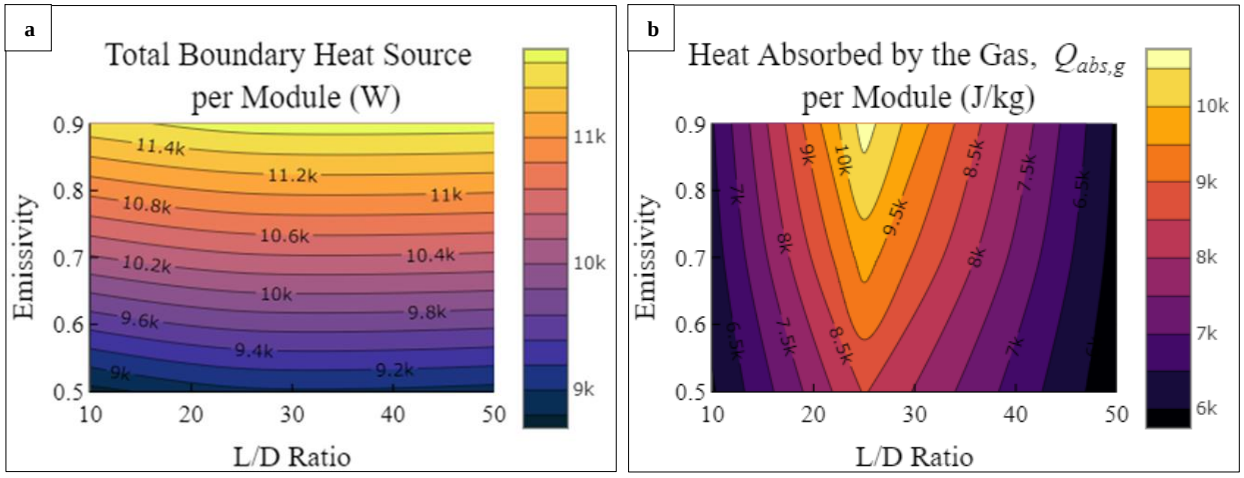

Figure 3.19: Analysis of key contributing energy streams for the base case – effect of L_{ch}

To avoid the sudden drop in efficiency with increased channel length, the length to diameter ratio will be left as is for the optimized case.

Table 3.4: Optimized base case receiver after second (and final) stage

Parameters & Responses	**Base Case Receiver**
Optimum design parameters	$(\varepsilon, R_{ch}, L_{ch}/D) = (0.8, 1[\text{mm}], 25)$
Exit gas temperature	820 K
Thermal efficiency	0.82
Volumetric effect ratio	0.85

3.3.2 Linear Reflectivity Distribution

3.3.2.1 Stage1 – Stepped Distribution

Figure 3.20 shows the results for the stepped distribution case with average emissivity in place of the reflective region length (L_e/L_{ch}) to make comparing to the base case results easier. Thermal efficiency and exit gas temperature increase with emissivity, similar to the base case. However, the maximum that occurs with porosity in the base case disappears here. Instead, lower porosities (or smaller channel radii) are favored for all values of average emissivity (or L_e/L_{ch}). Furthermore, the volumetric effect has a weaker dependence on emissivity. Nevertheless, the trend is, generally, the same (lower emissivity and porosity are favored, and the effect of porosity is more pronounced than the effect of emissivity). Also, none of the cases could achieve the volumetric effect.

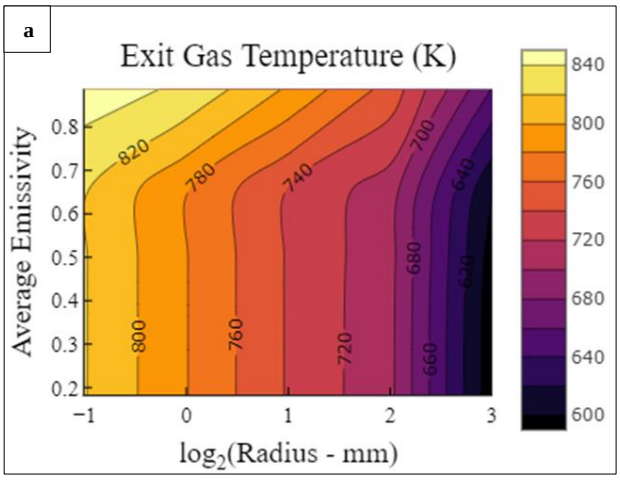

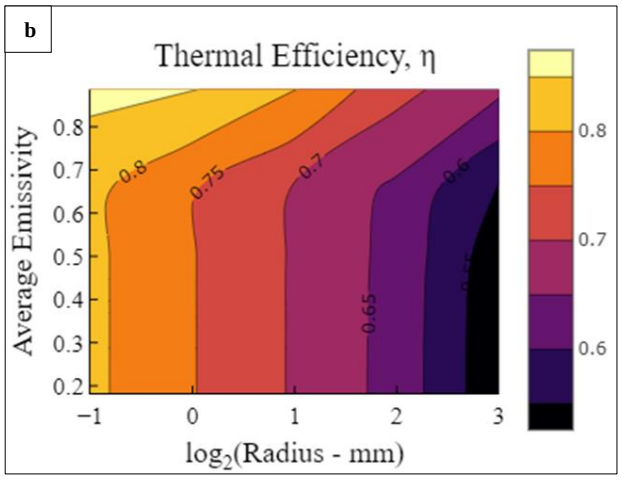

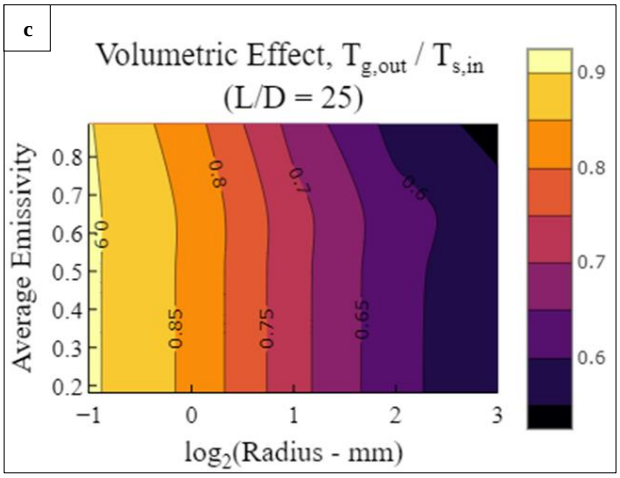

Plotted Independent Parameter	*Corresponding Independent Parameters*			
$\log_2(R_{ch})$	R_{ch} [mm]	ϕ	Re	Δp [Pa]
-1	0.5	0.309	32.4	42.90
0	1	0.510	39.2	13.70
1	2	0.694	57.6	5.50
2	4	0.826	96.8	2.68
3	8	0.907	176.4	1.46

Figure 3.20: Stepped distribution case parametric study – results for effect of average emissivity and porosity

To be able to perform a quantified comparison between the two cases, the ratio of each response in the stepped distribution case to responses in the base case is plotted. Contour lines for values greater than 1 indicate a region of improvement. Comparative results are in Figure 3.21 below. The figure shows that the greatest improvement in thermal efficiency and exit gas temperature occurs in regions of low emissivity and low porosity. These are, also, the regions with the largest improvement in boundary heat source (see Figure 3.22). This implies an improvement in radiation penetration in the stepped distribution case, which was the key conceptual motivator for this work.

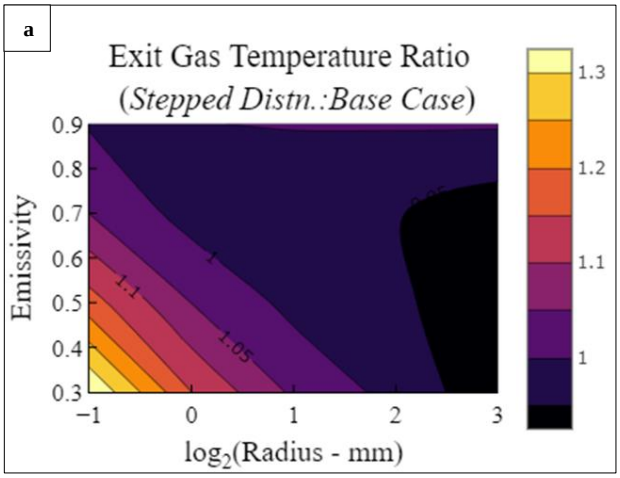

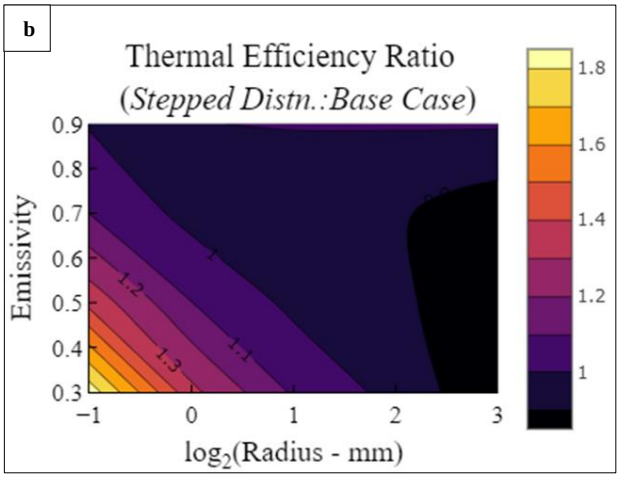

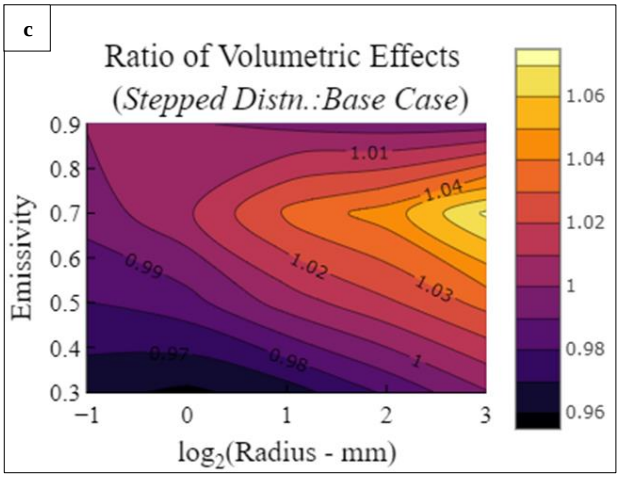

Plotted Independent Parameter	*Corresponding Independent Parameters*			
$\log_2(R_{ch})$	R_{ch} **[mm]**	ϕ	Re	Δp **[Pa]**
-1	0.5	0.309	32.4	42.90
0	1	0.510	39.2	13.70
1	2	0.694	57.6	5.50
2	4	0.826	96.8	2.68
3	8	0.907	176.4	1.46

Figure 3.21: Quantitative comparison between responses in stepped distribution case and base case

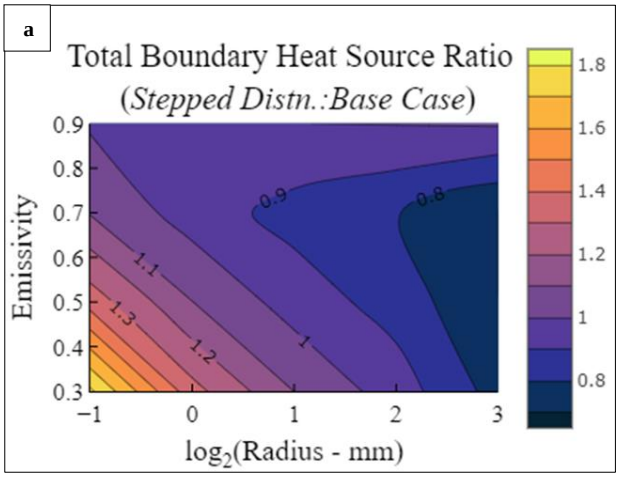

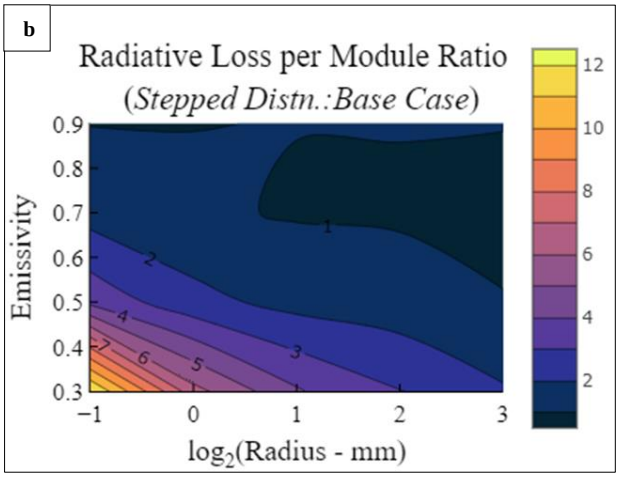

Figure 3.22: Quantitative comparison between key contributing fluxes in stepped distribution case and base case

Furthermore, the low emissivity, low porosity area corresponds to a slight decrement to the volumetric effect (Figure 3.21 (c)). The region with increased volumetric effect corresponds to the region with reduced radiative losses (or reduced frontal solid temperature).

There is no region that improves all three response parameters, (the contour lines for $[\eta]_{ratio} = 1$, $\left[T_{g,out}\right]_{ratio} = 1$, and $[E_{vol}]_{ratio} = 1$ are nearly the same. Instead, it is recommended to design each receiver based on their respective optimal performances. The maximum responses from each case (highest emissivity, and lowest porosity) cannot be directly compared since they essentially represent the same case of a uniform reflectivity receiver. Hence, the maximum responses for each case were selected for a given emissivity of 0.82 (the emissivity of Silicon carbide – the bulk material of the receiver). Because, compared to porosity, emissivity is a less flexible design parameter. At this emissivity, the optimum designs for each receiver are shown in Table 3.5 below. Also, these designs were optimized based on maximizing thermal efficiency and gas temperature only, because optimizing based on the volumetric effect ratio comes at a much higher cost the other two responses compared to the current scenario (where the volumetric effect ratio is no less than 95% its maximum possible value). The results in the table show a clear advantage to the linear reflectivity receiver for the given choice of receiver material.

Table 3.5: List of optimized designs for base case receiver and stepped distribution receiver based on SiC optical properties

Parameters & Responses	**Base Case Receiver**	**Stepped Distribution Receiver**
Optimum design parameters	$(\varepsilon, R_{ch}) = (0.8, 1\text{mm})$	$(L_e/L_{ch}, R_{ch}) = (0.15, 0.5\text{mm})$
Exit gas temperature	820 K	840 K
Thermal efficiency	0.82	0.89
Volumetric effect ratio	0.85	0.90

The optimized stepped distribution receiver design parameters ($(\varepsilon, R_{ch}) = (0.8,\ 0.5\text{mm})$) will be used in the next stage of the design which focuses on optimizing the channel length and exploring the effect of the distribution slope on the receiver performance.

3.3.2.2 Stage 2 – Graded Distribution

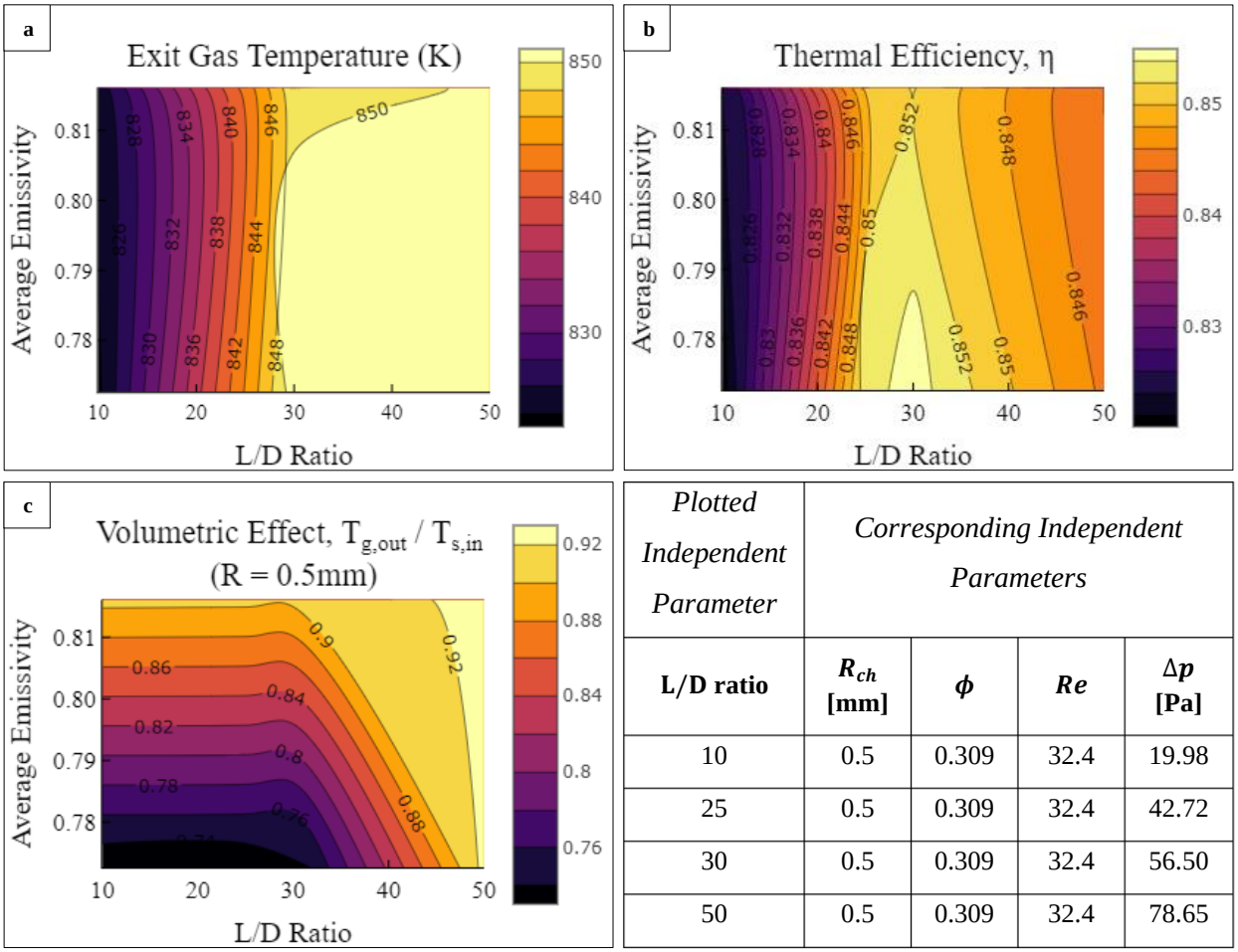

Plotted Independent Parameter	*Corresponding Independent Parameters*			
L/D ratio	**R_{ch} [mm]**	**ϕ**	**Re**	**Δp [Pa]**
10	0.5	0.309	32.4	19.98
25	0.5	0.309	32.4	42.72
30	0.5	0.309	32.4	56.50
50	0.5	0.309	32.4	78.65

Figure 3.23: Linear distribution case parametric study – results for effect of channel length and gradation slope

Figure 3.23 shows the responses plotted with average emissivity instead of slope on the y-axis. It is clear that a gradual slope has a negative effect on all responses, especially on the volumetric effect. Hence, the stepped distribution is more useful. Furthermore, it is clear that the effect of length on the responses has changed compared to the base case, so that the drop in efficiency with increased length is not as severe. Additionally, the volumetric effect and exit gas temperatures

continue increasing with channel length due to increased residence time, since the boundary heat source barely changes and the heat absorbed the gas follows the same trend as thermal efficiency.

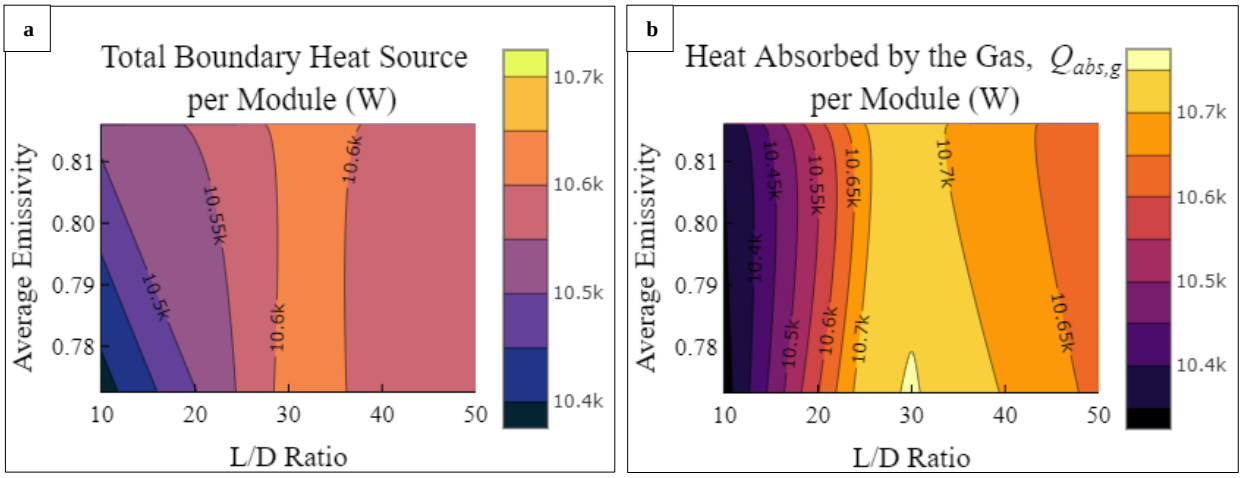

Figure 3.24: Analysis of key contributing energy streams for the linear distribution case – effect of L_{ch} and m

The drop in efficiency is fairly small compared to the effect on exit gas temperature and the volumetric effect. Therefore, the length to diameter ratio should be maximized to improve performance.

Table 3.6: List of optimized designs for base case receiver and graded distribution receiver based on SiC optical properties

Parameters & Responses	**Base Case Receiver**	**Graded Distribution Receiver**
Optimum design parameters	$(\varepsilon, R_{ch}) = (0.8, 1\text{mm})$	$(L_e/L_{ch}, R_{ch}, m, L_{ch}/D)$ $= (0.15, 0.5[\text{mm}], 1000[\text{m}^{-1}], 50)$
Exit gas temperature	820 K	850 K
Thermal efficiency	0.82	0.845
Volumetric effect ratio	0.85	0.92

3.3.3 Wall-Varied Reflectivity Distribution

3.3.3.1 Stage 1 – Effect of Axis Angle

Figure 3.25 shows the results for the first wall-varied distribution case where emissivity is only varied on $|y| = R_{ch}$ walls, with average emissivity in place of the y −wall emissivity to allow comparing trends with the base case. Similar trends to those observed for the stepped distribution case are seen here. The maximum with porosity feature that appears in the base case, disappears for both thermal efficiency and exit gas temperature. The volumetric effect becomes less dependent on emissivity, as well.

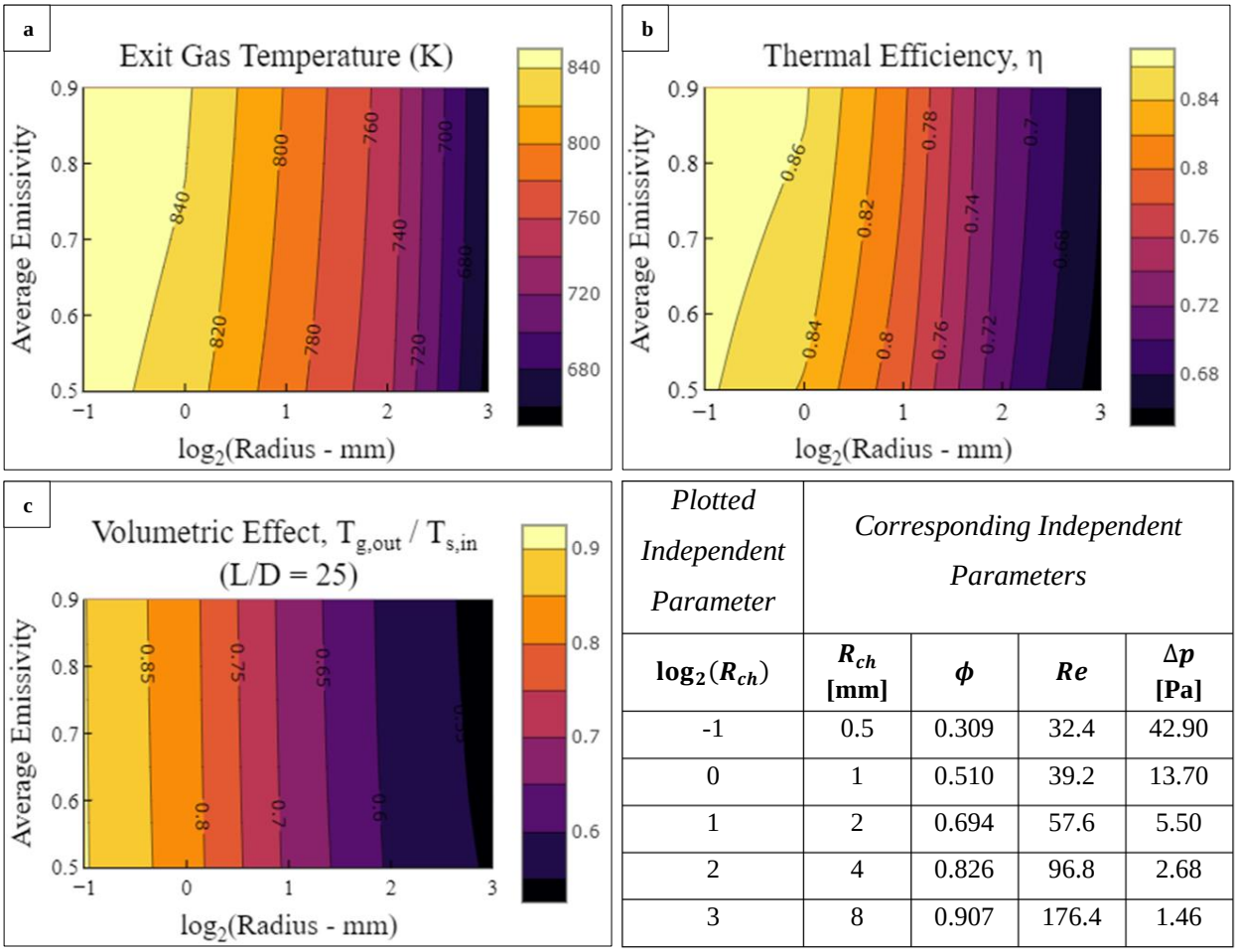

Plotted Independent Parameter	*Corresponding Independent Parameters*			
$\log_2(R_{ch})$	R_{ch} [mm]	ϕ	Re	Δp [Pa]
-1	0.5	0.309	32.4	42.90
0	1	0.510	39.2	13.70
1	2	0.694	57.6	5.50
2	4	0.826	96.8	2.68
3	8	0.907	176.4	1.46

Figure 3.25: Wall-varied distribution case parametric study – results for effect of average emissivity and porosity

More interestingly, the region that maximizes thermal efficiency and exit gas temperature becomes much larger. For example, $T_{g,out} = 840\text{K}$, in the base case, is only achievable for $\varepsilon > 0.8$ and $R_{ch} \leq 0.5\text{mm}$, while, here, it is achievable for $\varepsilon > 0.5$ and $R_{ch} \leq 1\text{mm}$. A quantitative comparison between this case and the base case (see Figure 3.26) shows that the exit gas temperature and thermal efficiency improve in the discrete wall distribution case for all combinations of emissivity and porosity, except at very high values of both. This region corresponds to the greatest increase in boundary heat source, as shown in Figure 3.27 below. It, also, corresponds to the greatest increase in radiative losses, but those have been shown to have a minor contribution compared to the boundary heat source.

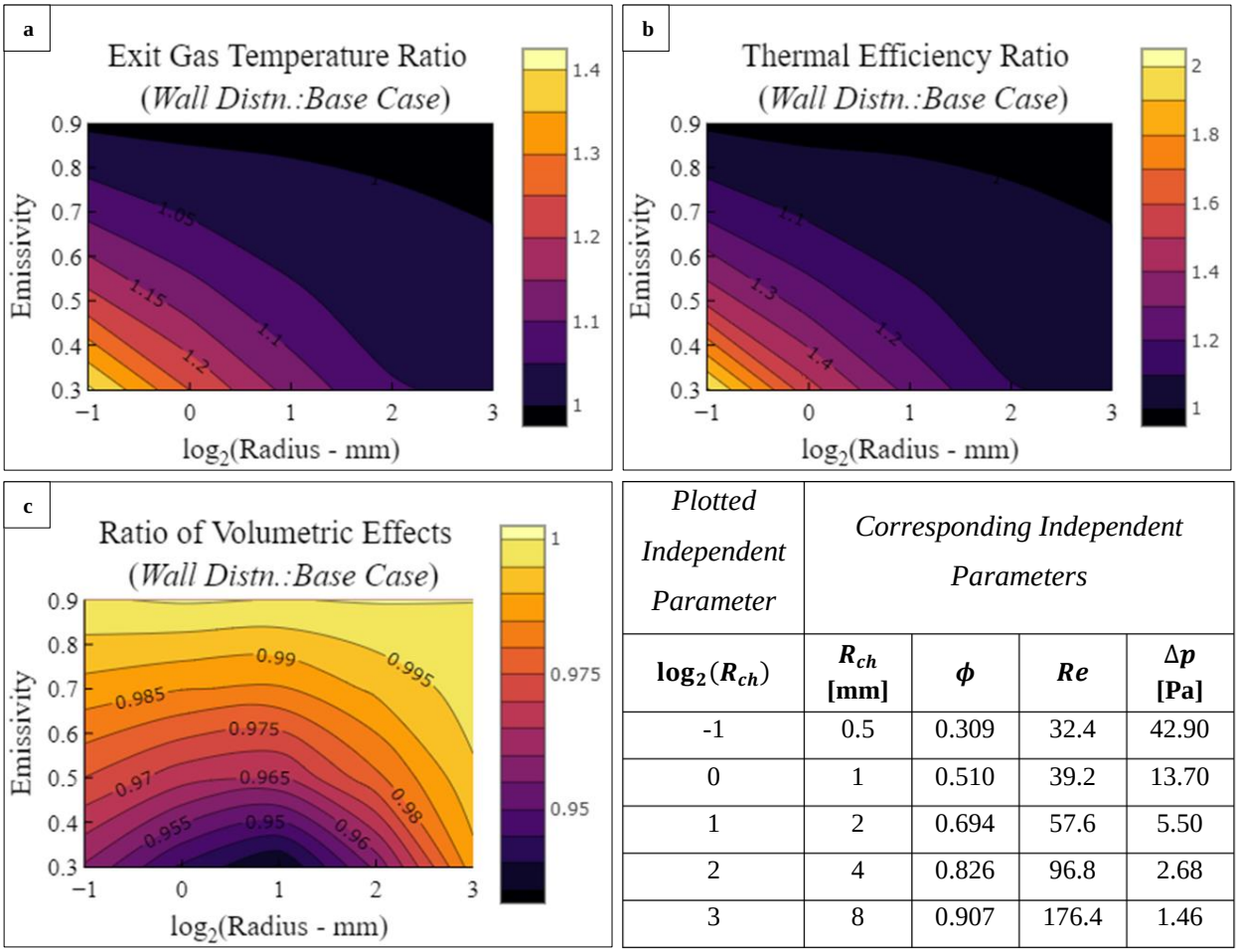

Plotted Independent Parameter	*Corresponding Independent Parameters*			
$\log_2(R_{ch})$	R_{ch} [mm]	ϕ	Re	Δp [Pa]
-1	0.5	0.309	32.4	42.90
0	1	0.510	39.2	13.70
1	2	0.694	57.6	5.50
2	4	0.826	96.8	2.68
3	8	0.907	176.4	1.46

Figure 3.26: Quantitative comparison between responses in wall-varied distribution case and base case

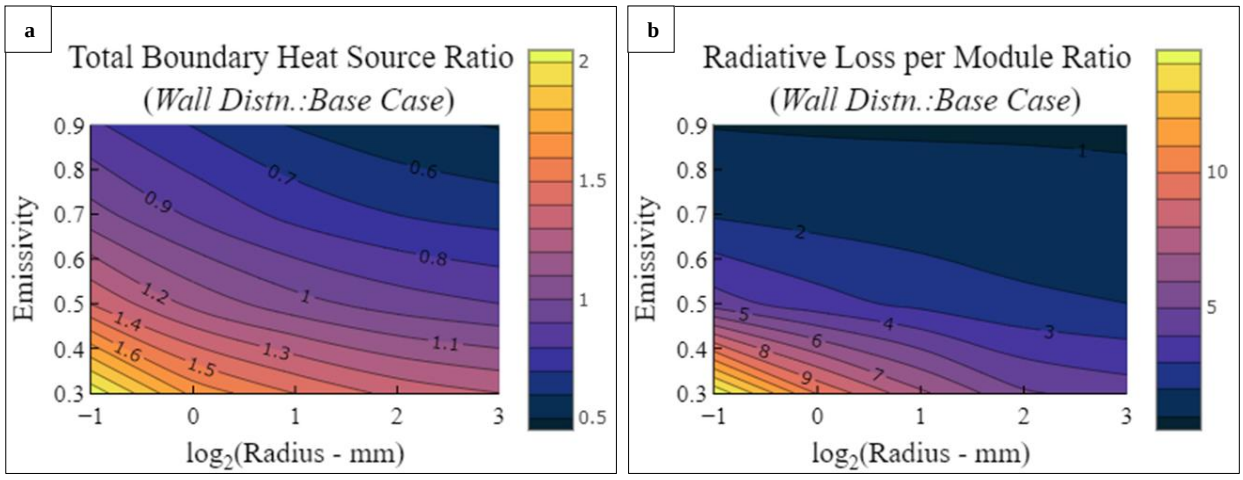

Figure 3.27: Quantitative comparison between key contributing fluxes in wall-varied distribution case and base case

The improved boundary heat source at lower porosities implies improved radiation penetration, but the increased radiative losses imply an increased frontal receiver temperature. The combined effect of these two phenomena on the volumetric effect explains why it decreases for nearly all combinations of porosity and emissivity (Figure 3.25 (c)).

Additionally, there is no region that improves all three responses at once and optimization is best to be carried out based on maximizing thermal efficiency and exit gas temperature at a given average emissivity. Thus, a similar procedure to the one used to optimize the stepped distribution case will be used here, after the effect of incidence angle is considered.

To study the effect of incidence angle, the parametric study was performed with reflectivity being varied for $|x| = R_{ch}$ walls only. These walls correspond to an off-axis angle 'θ_{axis}' (or incidence angle) of $23.5°$, while the results presented so far for $|y| = R_{ch}$ walls receive radiation at an off-axis angle of $10°$. The ratios of response parameters in the case $\theta_{axis} = 23.5°$ were plotted with respect to the previously analyzed results for $\theta_{axis} = 10°$. These results are shown in Figure 3.28 below.

The results show a slight increase in thermal efficiency and exit gas temperature, especially at $\log_2(R) = 0,\ \bar{\varepsilon} = 0.5$. The same trend is observed with the ratio of average solid temperatures (Figure 3.29 (c)). This occurs because the walls that receive radiation at a steeper angle ($|y| = R_{ch}$ walls), and consequently intercept more radiation, are left at a constant high absorptivity. This would, also, explain why the average solid temperature is higher despite the reduced boundary heat source (Figure 3.29 (a)).

Higher solid temperatures are expected for the case with a less steep off-axis angle, as more of the power on aperture will be incident on the

Furthermore, the volumetric effect increases when reflectance is varied on the walls that receive radiation at a steeper angle of 10°. Because a radiation coming from a lamp at a steeper off-axis angle has a better chance of intersecting the interior walls of the receiver and increasing the reflectivity of those walls will improve radiation penetration more significantly. This is confirmed by the contour plot for the ratio of boundary heat sources (Figure 3.29 (a)), where the boundary heat source increases when reflectance is varied on the walls that receive radiation at a steeper angle of 10°.

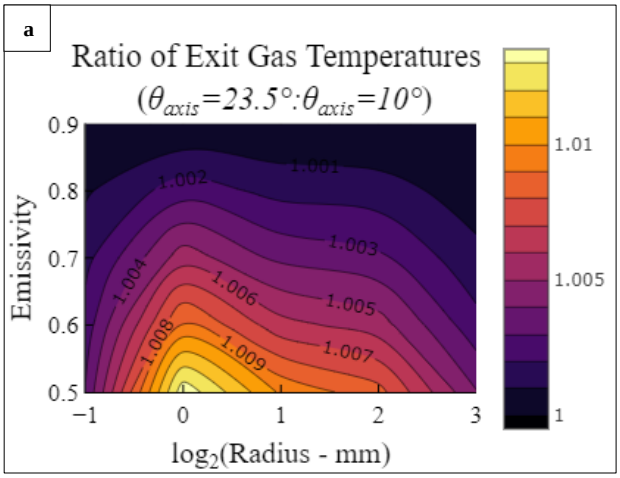

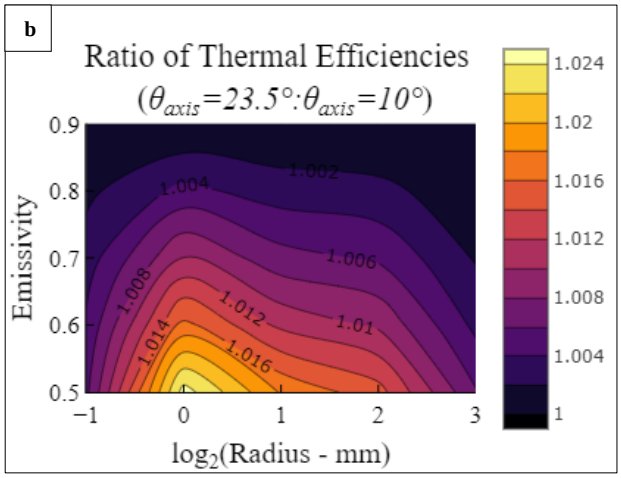

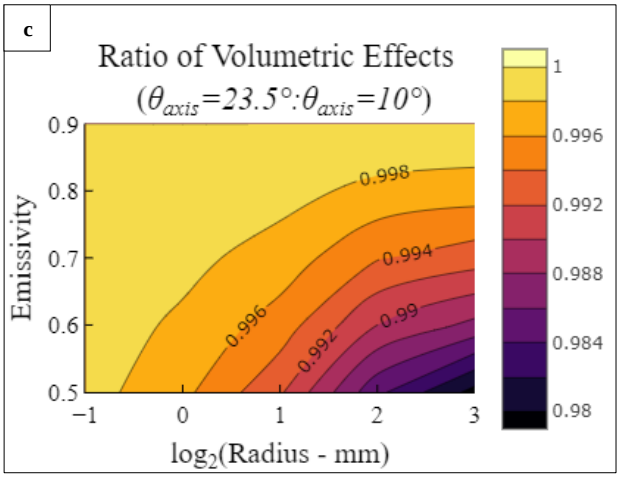

Plotted Independent Parameter	*Corresponding Independent Parameters*			
$\log_2(R_{ch})$	R_{ch} [mm]	ϕ	Re	Δp [Pa]
-1	0.5	0.309	32.4	42.90
0	1	0.510	39.2	13.70
1	2	0.694	57.6	5.50
2	4	0.826	96.8	2.68
3	8	0.907	176.4	1.46

Figure 3.28: Quantitative assessment of the effect of off-axis angle on the responses for the wall-varied distribution case

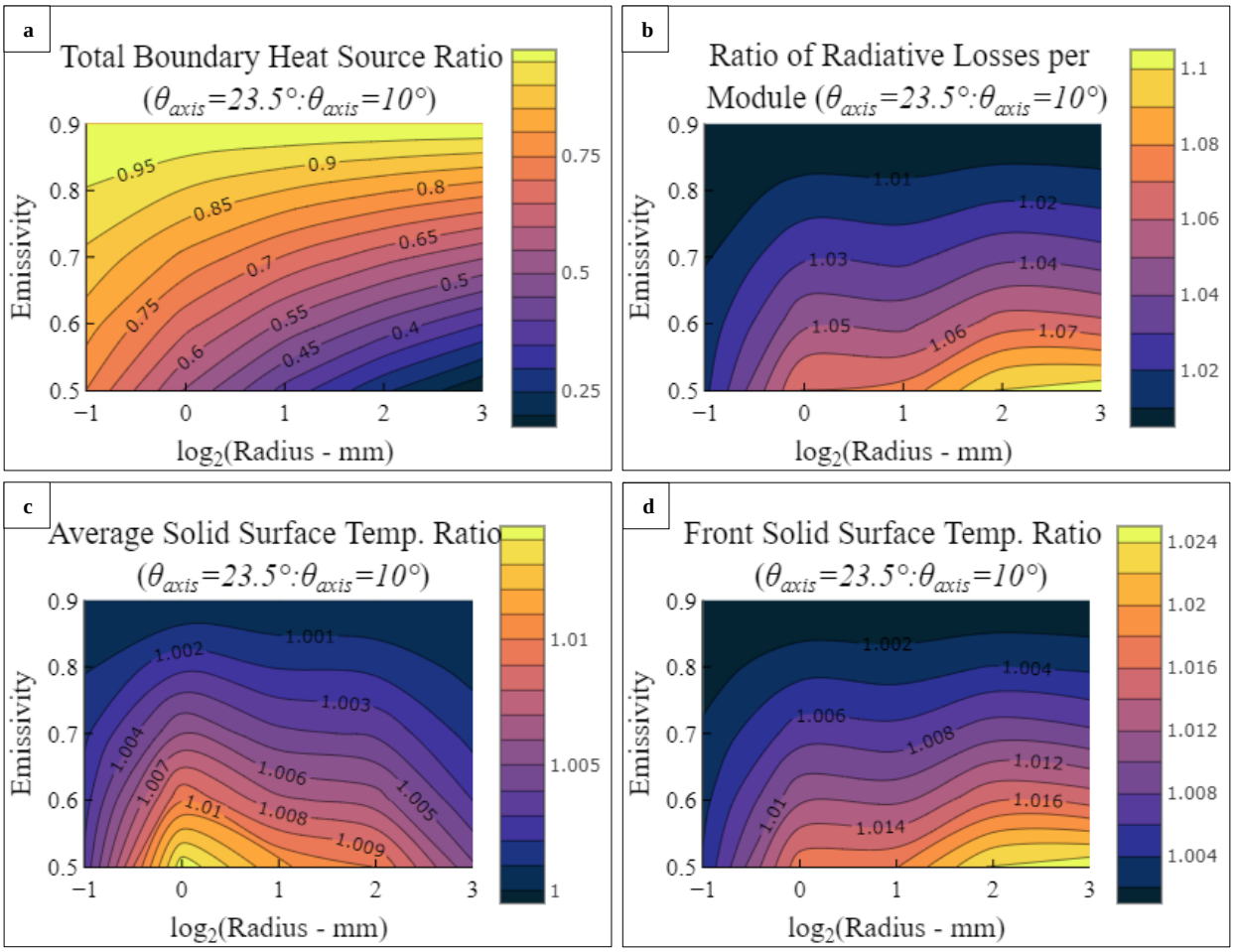

Figure 3.29: Quantitative assessment of the effect of off-axis angle on the key contributing fluxes for the wall-varied distribution case

From this, it is clear that varying emissivity on the $|x| = R_{ch}$ walls, which receive radiation at a larger off-axis angle, is more advantageous, as it improves thermal efficiency and exit gas temperature at a minimal cost to the volumetric effect (drop in E_{vol} in the region of interest is less than 0.2%). Hence, the parameters that will be used for the next stage correspond to the emissivity of SiC and are as in Table 3.7 below.

Table 3.7: List of optimized designs for base case receiver and wall-varied distribution receiver based on SiC optical properties

Parameters & Responses	**Base Case Receiver**	**Wall-Varied Receiver**
Optimum design parameters	$(\varepsilon, R_{ch}) = (0.8, 1\text{mm})$	$(\alpha_x, \alpha_y, R_{ch}) = (0.7, 0.9, 0.5\text{mm})$

Table 3.7: List of optimized designs for base case receiver and wall-varied distribution receiver based on SiC optical properties (Continued)

Parameters & Responses	Base Case Receiver	Wall-Varied Receiver
Exit gas temperature	820 K	855 K
Thermal efficiency	0.82	0.87
Volumetric effect ratio	0.85	0.90

3.3.3.2 Stage 2 – Effect of Channel Length

Figure 3.30below shows how the responses change with channel length for the case selected in the previous section (see Table 3.7). Exit gas temperature and the volumetric effect seem to be positively affected by increased channel length. This can be attributed to an increase in contact time between the gas and solid, since the change in the boundary heat source with channel length is more or less negligible (see Figure 3.31 (a)). On the other hand, A maximum for efficiency vs. length is observed with a corresponding maximum for Q_{abs} (Figure 3.31 (b)). This loss in the rate of convective transport can be attributed to the increased pressure drop. Even though longer channels achieve a higher gas exit temperature, they, also, increase the inlet gas temperature, which should explain why Q_{abs} decreases while $T_{g,out}$ increases.

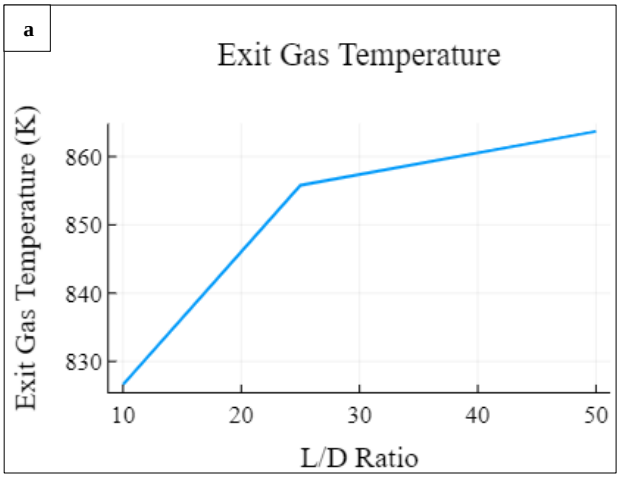

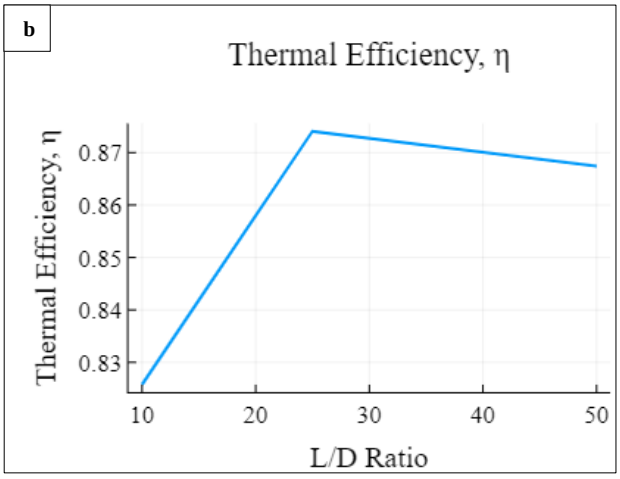

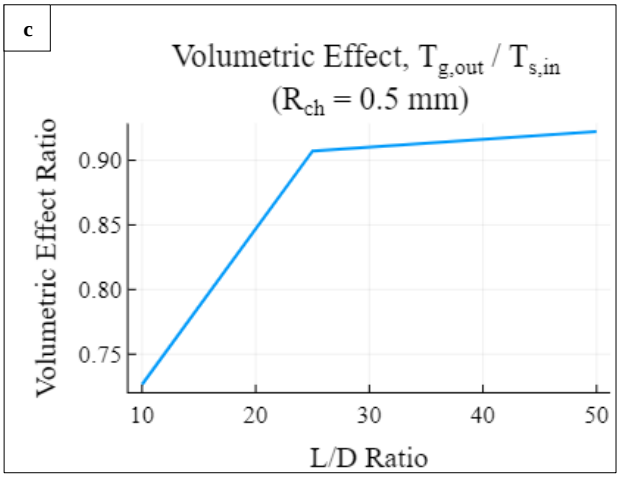

Plotted Independent Parameter	*Corresponding Independent Parameters*			
L/D ratio	**R_{ch} [mm]**	**ϕ**	**Re**	**Δp [Pa]**
10	0.5	0.309	32.4	19.98
25	0.5	0.309	32.4	42.72
50	0.5	0.309	32.4	78.65

Figure 3.30: Wall-varied distribution case parametric study – effect of channel length

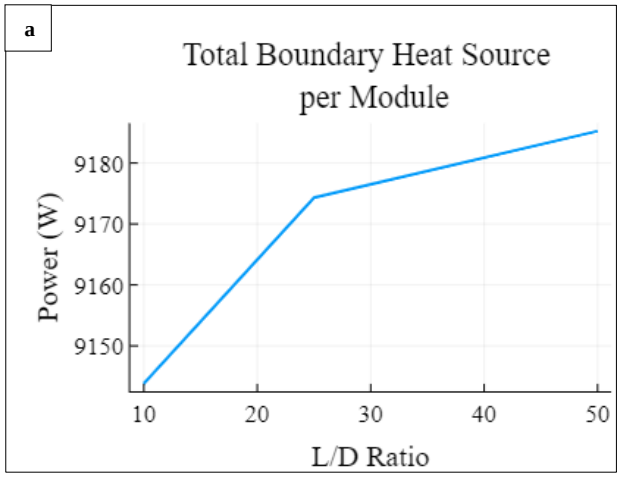

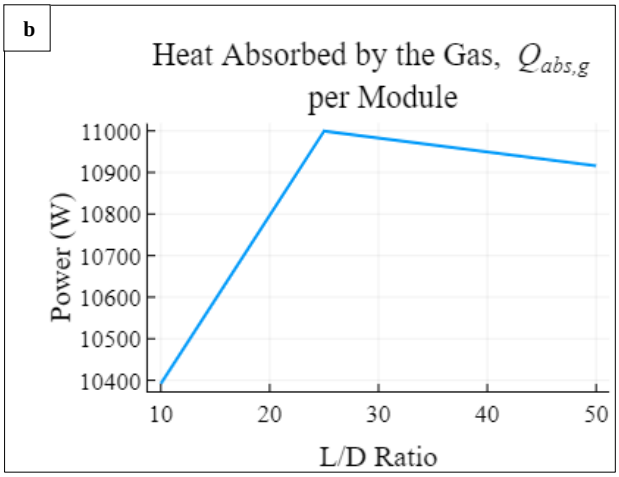

Figure 3.31: Analysis of key contributing energy streams for the wall-varied distribution case – effect of L_{ch}

The drop in efficiency is fairly small compared to the effect on exit gas temperature and the volumetric effect. Therefore, the length to diameter ratio should be maximized to improve performance.

Table 3.8: List of optimized design for base case receiver and wall-varied distribution receiver based on SiC optical properties – final stage

Parameters & Responses	**Base Case**	**Wall-Varied Receiver**
Optimum design parameters	$(\varepsilon, R_{ch}, L_{ch}/D)$ $= (0.8, 1[\text{mm}], 25)$	$(\alpha_x, \alpha_y, R_{ch}, L_{ch}/D)$ $= (0.7, 0.9, 0.5[\text{mm}], 50)$
Exit gas temperature	820 K	863 K
Thermal efficiency	0.82	0.87
Volumetric effect ratio	0.85	0.92

4. Conclusion

In summary, a honeycomb volumetric receiver was modelled using two approaches – a finite differences model that is 1-D in the gas phase and a finite element model that is 3-D in both the gas and solid phases. The initial FDM model attempt could not be successfully completed because of the required addition of a momentum transfer model which would have greatly increased the computational effort.

The developed FEM model, on the other hand, was somewhat successful in recreating the results of the reference literature case, as the source of the error was identified as unreported material properties and inconsistently reported operating conditions. But, the exact required combination to achieve the published results was not found.

Nevertheless, the FEM model was used to model 3 cases to study the effect of reflectivity distribution on the performance of a volumetric receiver. A summary of the results of those studies is shown in Table 4.1 below. It shows that applying varied reflectivity improves all three responses compared to the base case, which happens to have dimensions equivalent to the HiTRec-II. Applying a discrete varied reflectivity to each wall is the configuration that improves the overall performance the most.

Table 4.1: Summary of sensitivity analysis results

Receiver Case	**Base Case**	**Graded Reflectivity**	**Wall-Varied Receiver**
Optimum Design Parameters			
Channel radius	$R_{ch} = 1[\text{mm}]$	$R_{ch} = 0.5[\text{mm}]$	$R_{ch} = 0.5[\text{mm}]$
Optical properties	$\varepsilon = 0.8$	$L_e/L_{ch} = 0.15$	$\alpha_y = 0.9$
	-	$m = 1000[\text{m}^{-1}]$	$\alpha_x = 0.7$
Channel length	$L_{ch}/D = 25$	$L_{ch}/D = 50$	$L_{ch}/D = 50$

Table 4.1: Summary of sensitivity analysis results (Continuted)

Receiver Case	**Base Case**	**Graded Reflectivity**	**Wall-Varied Receiver**
Response Parameters			
Exit gas temperature	820 K	850 K	863 K
Thermal efficiency	0.82	0.845	0.87
Volumetric effect ratio	0.85	0.92	0.92

5. Future Work

5.1 Numerical Optimization

The results of the preformed parametric studies give good insight into the behavior of the system and the key regions of interest. These insights can be used to execute an optimization study on the system, where all parameters are considered at once and a better resolution of the behavior can be obtained. This can be completed using COMSOL itself, either using COMSOL's optimization packages or coupling the COMSOL solver to a higher performing optimization algorithm using a low-level language. This, however, is secondary in importance to the experimental validation.

5.2 Experimental Validation

As discussed in section 3.2.1, the developed FEM model could not be verified using literature data because of a combination of unreported material properties and inconsistency in the provided operating conditions. Thus, experimental validation is necessary.

The typical method for validating volumetric receivers is to construct the entire monolith and perform experiments using that. However, this approach is not achievable for this project. Because of limitations on the achievable aperture area in the available solar furnace facilities at TAMUQ and because of the effort involved in developing a method for coating the interior walls of a monolith. Instead, validation is planned in 2 stages, where the first stage uses a single insulated channel is in place of the volumetric receiver and the second stage uses the manufactured full-scale monolith. If the experimental results of stage 1 indicate a good agreement with simulation results, then the effort of manufacturing a full-scale varied reflectance monolithic receiver will be justified.

Figure 5.1 shows a schematic of the system designed for the first stage of validation. An insulated square or hexagonal SiC channel receives radiation from a high flux solar simulator and is connected from the back to a cylindrical alumina pipe through a ceramic connector piece. The back of the cylindrical alumina extension pipe is sealed onto a stainless-steel pipe that directs the exit gas to a cooling coil before it enters the mass flow controller (MFC). To measure the actual exit gas temperature from the receiver, a thermocouple is inserted axially through the alumina extension pipe and exits through a sealed port in the stainless-steel pipe.

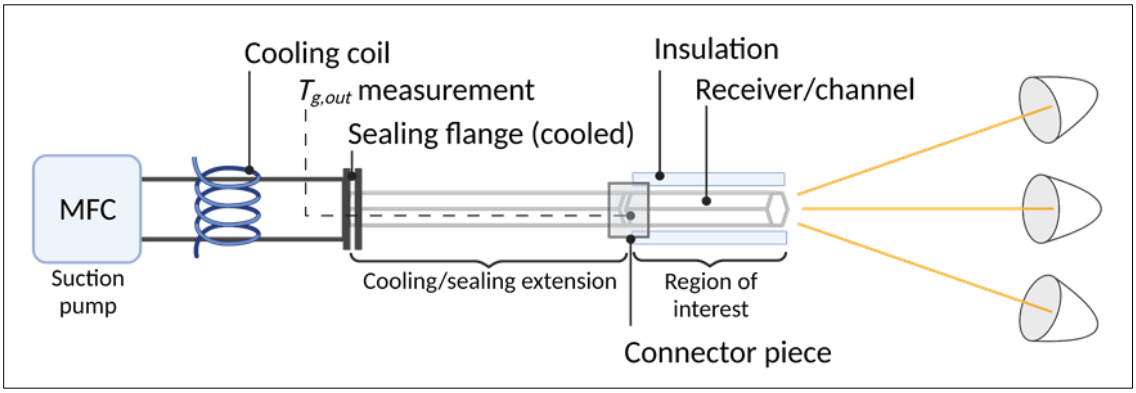

Figure 5.1: Schematic of first stage of validation setup

The only parts of this system that are unavailable are the receiver channel and connector piece assembly. This has already been ordered for manufacture with the materials and dimensions indicated in the CAD drawing shown in Figure 5.2. The dimensions of the ordered pieces were selected before optimized designs were arrived at and the effects of large channel length and large channel radius were not known. Nevertheless, channel length can be adjusted by machining the parts as necessary and the final physical dimensions can be used to run new simulation results for validation.

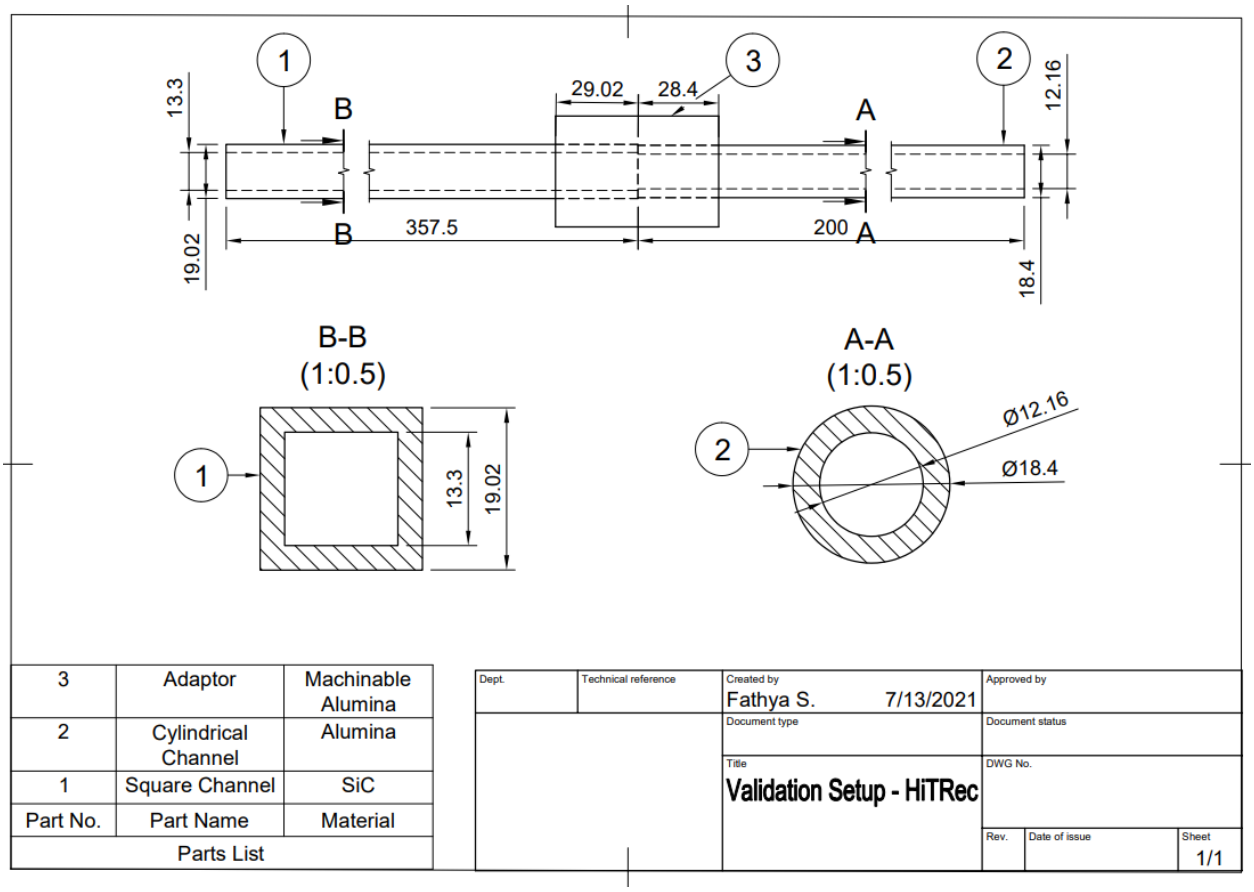

Figure 5.2: CAD drawing for receiver assembly needed for first stage of validation (mm units)

To manufacture the varied-reflectivity channel receiver, the plan is manufacture sheets of the base ceramic material and apply the desired reflectance to the planar form of the material. The channel can, then, be assembled from sides cut and machined from the desired reflectivity planar material.

The receiver material considered for now is MAX-phase Ti_2SiC_3 ceramic, which exhibit properties between those of metals and ceramics. The most relevant properties are that they exhibit high thermal and chemical stability like ceramics, but can be polished to a metal-like shine (Sarwar *et al.*, 2018).

6. References

Alberti, F. *et al.* (2016) 'Numerical analysis of radiation propagation in innovative volumetric receivers based on selective laser melting techniques', *AIP Conference Proceedings*, 1734(May 2016). doi: 10.1063/1.4949053.

Ali, M. *et al.* (2020) 'Consistent coupled optical and thermal analysis of volumetric solar receivers with honeycomb absorbers', *Renewable Energy*. Elsevier Ltd, 145, pp. 1849–1861. doi: 10.1016/j.renene.2019.07.082.

Alxneit, I. and Dibowski, G. (2011) *R12.5 Solar Simulator Evaluation Report - Project SFERA*. doi: 10.13140/RG.2.2.17337.06243.

Ávila-Marín, A. L. (2011) 'Volumetric receivers in Solar Thermal Power Plants with Central Receiver System technology: A review', *Solar Energy*, 85(5), pp. 891–910. doi: 10.1016/j.solener.2011.02.002.

Avila-Marin, A. L., Alvarez de Lara, M. and Fernandez-Reche, J. (2018) 'Experimental results of gradual porosity volumetric air receivers with wire meshes', *Renewable Energy*. Elsevier Ltd, 122, pp. 339–353. doi: 10.1016/j.renene.2018.01.073.

Bird, R. byron, Stewart, W. E. and Lightfoot, E. N. (2002) *Transport Phenomena*. 2nd editio. New York: John Wiley & Sons Inc.

Capuano, R. *et al.* (2016) 'Numerical models of advanced ceramic absorbers for volumetric solar receivers', *Renewable and Sustainable Energy Reviews*. Elsevier, 58, pp. 656–665. doi: 10.1016/j.rser.2015.12.068.

Capuano, R. *et al.* (2017) 'Optimized volumetric solar receiver: Thermal performance prediction

and experimental validation', *Renewable Energy*. Elsevier Ltd, 114, pp. 556–566. doi: 10.1016/j.renene.2017.07.071.

COMSOL Multiphysics® (2020a) *CFD Module User 's Guide*, *COMSOL Documentation*. Stockholm, Sweden: COMSOL AB.

COMSOL Multiphysics® (2020b) *Heat Transfer Module: User's Guide*, *COMSOL Documentation*. Stockholm, Sweden: COMSOL AB.

Du, S. *et al.* (2020) 'Experiment and optimization study on the radial graded porous volumetric solar receiver matching non-uniform solar fl ux distribution', *Applied Energy*. Elsevier, 275(May), p. 115343. doi: 10.1016/j.apenergy.2020.115343.

Du, S., Ren, Q. and He, Y. L. (2017) 'Optical and radiative properties analysis and optimization study of the gradually-varied volumetric solar receiver', *Applied Energy*. Elsevier Ltd, 207, pp. 27–35. doi: 10.1016/j.apenergy.2017.05.165.

Gillies, D. F. (2018) *Lecture 13 : Radiosity - Principles*, *Department of Computing Imperial College of London*. Available at: https://www.doc.ic.ac.uk/~dfg/graphics/graphics2010/GraphicsLecture13.pdf (Accessed: 3 September 2021).

Gomez-Garcia, F. *et al.* (2015) 'Numerical analysis of radiation propagation in a multi-layer volumetric solar absorber composed of a stack of square grids', *Solar Energy*, 121, pp. 94–102. doi: 10.1016/j.solener.2015.04.047.

Ho, C. K. (2017) 'Advances in central receivers for concentrating solar applications', *Solar Energy*. Elsevier Ltd, 152, pp. 38–56. doi: 10.1016/j.solener.2017.03.048.

Hoffschmidt, B. *et al.* (2003) 'Performance evaluation of the 200-kWth HiTRec-II open

volumetric air receiver', *Journal of Solar Energy Engineering, Transactions of the ASME*, 125(1), pp. 87–94. doi: 10.1115/1.1530627.

Incropera, F. P. *et al.* (2007) *Fundamentals of Heat and Mass Transfer*. Sixth edit. John Wiley & Sons, Inc.

Köberle, A. C., Gernaat, D. E. H. J. and van Vuuren, D. P. (2015) 'Assessing current and future techno-economic potential of concentrated solar power and photovoltaic electricity generation', *Energy*, 89, pp. 739–756. doi: 10.1016/j.energy.2015.05.145.

Kribus, A. *et al.* (2014) 'The promise and challenge of solar volumetric absorbers', *Solar Energy*, 110, pp. 463–481. doi: 10.1016/j.solener.2014.09.035.

Luque, S. *et al.* (2018) 'Exploiting volumetric effects in novel additively manufactured open solar receivers', *Solar Energy*. Elsevier, 174(September), pp. 342–351. doi: 10.1016/j.solener.2018.09.030.

Modest, M. F. (2013) *Radiative Heat Transfer*. 3rd editio. New York, United States: Elsevier Inc.

Munro, R. G. (1997) 'Material properties of a sintered α-SiC', *Journal of Physical and Chemical Reference Data*, 26(5), pp. 1195–1203. doi: 10.1063/1.556000.

Nakakura, M. *et al.* (2018) 'Conjugate radiation-convection-conduction simulation of volumetric solar receivers with cut-back inlets', *Solar Energy*. Elsevier, 170(December 2017), pp. 606–617. doi: 10.1016/j.solener.2018.06.006.

Pabst, C. *et al.* (2017) 'Experimental performance of an advanced metal volumetric air receiver for Solar Towers', *Renewable Energy*. Elsevier Ltd, 106, pp. 91–98. doi: 10.1016/j.renene.2017.01.016.

Rackauckas, C. and Nie, Q. (2017) 'Differentialequations.jl -- a performant and feature-rich

ecosystem for solving differential equations in julia', *Journal of Open Research Software*, 5(1).

Reddy, J. and Gartling, D. (2010) 'The Finite Element Method', in *The Finite Element Method in Heat Transfer and Fluid Dynamics*. Bosa Roca: Taylor & Francis Group, pp. 43–86.

Sarwar, J. *et al.* (2015) 'Experimental and numerical investigation of the aperture size effect on the efficient solar energy harvesting for solar thermochemical applications', *Energy Conversion and Management*. Elsevier Ltd, 92, pp. 331–341. doi: 10.1016/j.enconman.2014.12.065.

Sarwar, J. *et al.* (2018) 'Characterization of thermal performance, flux transmission performance and optical properties of MAX phase materials under concentrated solar irradiation', *Solar Energy Materials and Solar Cells*. North-Holland, 182, pp. 76–91. doi: 10.1016/J.SOLMAT.2018.03.018.

Sedighi, M. *et al.* (2020) 'Design of high-temperature atmospheric and pressurised gas-phase solar receivers: A comprehensive review on numerical modelling and performance parameters', *Solar Energy*. Elsevier, 201(February), pp. 701–723. doi: 10.1016/j.solener.2020.03.025.

Turgut, O. and Sarı, M. (2013) 'Experimental and numerical study of turbulent flow and heat transfer inside hexagonal duct', *Heat and Mass Transfer*, 49(4), pp. 543–554. doi: 10.1007/s00231-012-1101-z.

Usman, S. and Ozalp, N. (2012) 'NUMERICAL AND OPTICAL ANALYSIS OF WEATHER ADAPTABLE SOLAR REACTOR', in *9th International Conference on Heat Transfer, Fluid Mechanics and Thermodynamics*. Malta.

Yu, D.-M. *et al.* (2021) 'A novel multilayer high temperature solar absorber coating based on high-entropy alloy NbMoTaW: Optical properties, thermal stabilityand corrosion properties', *Journal of Materiomics*, 7, pp. 895–903.